

---

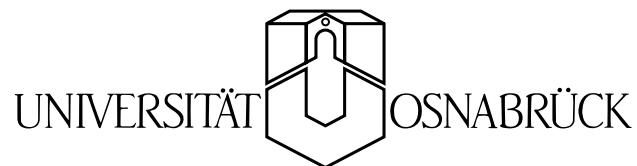
# **Optical and Dielectric Properties of $\text{Sr}_x\text{Ba}_{1-x}\text{Nb}_2\text{O}_6$**

---

Dissertation zur Erlangung des Grades  
Doktor der Naturwissenschaften

von  
Călin A. David

vorgelegt dem Fachbereich Physik der



im Dezember 2004

# Contents

<b>1</b>	<b>Introduction</b>	<b>1</b>
<b>2</b>	<b>Theoretical Background</b>	<b>3</b>
2.1	Growth and Structure of Strontium Barium Niobate . . . . .	3
2.2	Optical Properties . . . . .	5
2.2.1	Interband Transitions and Band Edge Absorption . . . . .	5
2.2.2	Vibrational Transitions and Infrared Absorption . . . . .	8
2.2.3	The Raman Effect . . . . .	11
2.3	Dielectric Properties . . . . .	15
2.3.1	Polarization, Pyroelectricity . . . . .	15
<b>3</b>	<b>Optical Properties</b>	<b>17</b>
3.1	Band Edge Absorption . . . . .	17
3.1.1	Experimental Method, Omega 10 Spectrophotometer . . . . .	17
3.1.2	Results and Discussion . . . . .	18
3.2	OH <sup>-</sup> stretching vibration . . . . .	23
3.2.1	FT-IR Spectrometer . . . . .	23
3.2.2	OH <sup>-</sup> doping . . . . .	25
3.2.3	Results, Data Fiting and Discussion . . . . .	28
3.3	Raman Spectroscopy . . . . .	37
3.3.1	Experimental setup . . . . .	37
3.3.2	Group Theoretical Considerations for Lattice Vibrations . . . . .	37
3.3.3	Results and Discussion . . . . .	40
<b>4</b>	<b>Dielectric Properties</b>	<b>47</b>
4.1	Pyroelectric Measurement . . . . .	47
4.1.1	Experimental setup . . . . .	47

4.1.2 Results and discussion . . . . .	48
<b>5 Conclusions and Summary</b>	<b>55</b>
<b>A Dielectric spectroscopy</b>	<b>57</b>
<b>Literature</b>	<b>60</b>

# Chapter 1

## Introduction

Strontium barium niobate  $\text{Sr}_x\text{Ba}_{1-x}\text{Nb}_2\text{O}_6$  (SBN with  $x=0.61$  for the congruent composition) was synthesized and identified as a ferroelectric crystal at room temperature in the 1960s [1]. Due to its outstanding photorefractive, electro-optic, nonlinear optic, and dielectric properties, SBN is a very attractive material for technological applications and basic research. Therefore, SBN is used in applications such as pyroelectric detectors [2, 3], holographic data storage systems [4, 5, 6, 7], phase conjugation [8], generation of photorefractive solitons [9], quasi-phase-matched second-harmonic generation [10], and electro-optic modulation [11].

The exceptional properties of the SBN crystal have drawn the attention of scientists; a number of studies have been carried out and many are still in progress. In the literature are several articles concerning the SBN crystal, especially on the congruently melting composition. It is known that the existence region for the tetragonal tungsten-bronze structure of strontium barium niobate is in the range 0.26 to 0.87 [12].

The aim of the current work was to investigate several properties of the material in the whole composition range where the crystal can be grown. Within the programme of the "Graduate College 695", a crystal grower team has grown SBN crystals in the entire range, so all necessary samples were available.

The methods used in this dissertation to analyze several SBN properties as a function of composition are: Band edge absorption, Infrared absorption, Raman scattering and pyroelectric measurement.

## Outline of the Dissertation

This dissertation consists of five chapters. Chapter 1 presents a general introduction and motivation of the research.

In the beginning of the second chapter a description of the SBN crystal was made. After that we introduce some basic theories regarding the optical and dielectric properties.

The next two chapters are the main part of this dissertation, which presents the experimental setups, results and discussions. The experiments are divided into two parts: optical properties are presented in chapter 3 and dielectric properties in chapter 4. The main purpose of the experiments was to determine the dependence of the measured property on the crystal composition.

The optical measurements presented in chapter 3 are: Composition and temperature dependence of the band edge. A Fourier-Transform-Infrared Spectrometer ( FT-IR ) was used to investigate the OH stretching mode at room temperature. Raman spectroscopy served as a tool to study the dependence of the lattice vibration on composition.

In the fourth chapter we describe a complete investigation of the phase-transition temperature using pyroelectric measurements.

The main results are concluded in the last chapter.

This thesis ends with an appendix where a description of the dielectric spectroscopy setup is given which has been developed.

# Chapter 2

## Theoretical Background

### 2.1 Growth and Structure of Strontium Barium Niobate

All SBN crystals were grown by Dr. Rainer Pankrath and Dr. Michael Ulex at the Crystal Growth Laboratory of the Physics Department at the University of Osnabrück. The Czochralski method was used to grow these crystals. A few of the technical data of this method are: the vertical temperature gradient in the furnace was about  $1^\circ\text{C}/\text{cm}$ , the seed crystal was air-cooled and continuously rotated with 28 cycles per minute and the crystal are grown in the  $c$ -direction and pulled out with a speed of 0.4 to 0.8 mm/h [12].

SBN crystals belong to the tetragonal unfilled tungsten-bronze (TB) structure with the space group  $P4bm$ . Tungsten bronze material have a general chemical formula given by  $(A1)_4(A2)_2C_4(B1)_2(B2)_8O_{30}$ . The SBN structure is built up of two types of crystallographically independent  $\text{NbO}_6$  octahedra linked by their corners in such a way that three different types of channels are formed along the tetragonal  $c$  axis [14, 15, 16, 17, 18]. One, a triangle channel (C in Fig. 2.1 and 2.2), is always empty, the second, a tetragonal channel, is partially filled only by Sr atoms (A2), while the third one, a pentagonal channel, is also partially occupied by Sr and Ba (A1).

According to the phase diagram, the existence region of the tetragonal tungsten-bronze structure of  $\text{Sr}_x\text{Ba}_{1-x}\text{Nb}_2\text{O}_6$  is found to be  $0.26 < x < 0.87$  [12]. Chernaya et al. [16] studied the structure of a SBN crystal with  $x = 0.61$  and compared with a the data

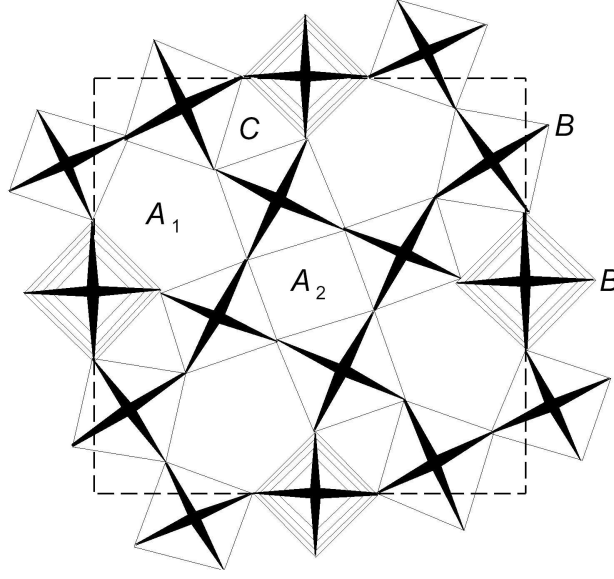


Figure 2.1: The tungsten-bronze type structure projected to the (001) plane [13]

obtained for single crystals of the compositions  $x = 0.33$  and  $x = 0.75$  [14, 15]. They found that the crystal structure of SBN is a partially-filled one. It was demonstrated that the tetragonal channels are occupied only by Sr up to 70.5%, 72.5%, 82.2% for  $x = 0.33$ ,  $x = 0.61$ ,  $x = 0.75$ , respectively. The large channels (five-fold channels) are occupied by Ba and Sr atoms in different concentrations, depending on the composition  $x$ . For  $x = 0.33$  (Sr poor) the five-fold channels are occupied only by Ba 84% and for  $x = 0.75$  (Sr rich) the channel is randomly occupied by the Ba and Sr atoms with a total occupancy factor of 84.7% (34.4% Ba and 50.3% Sr).

The units cell parameters vary almost linearly with composition,  $a = 12.448$  to  $12.412$  Å and  $c = 3.974$  to  $3.905$  Å for  $x = 0.32$  to  $0.82$  [19].

The Curie temperatures ( $T_c$ ) of the SBN crystals are in the range  $10 - 225^\circ\text{C}$  for  $x = 0.82 - 0.32$  respectively [20]. Below  $T_c$  the crystals are in a ferroelectric phase with the point group  $4mm$ . The transition from the ferroelectric into the paraelectric phase will bring the crystal into a centrosymmetric phase with the point group  $4/mmm$ . The ferroelectric domains of the crystal are always parallel or antiparallel to the crystallographic  $c$  axis, allowing only two equivalent polarization directions.

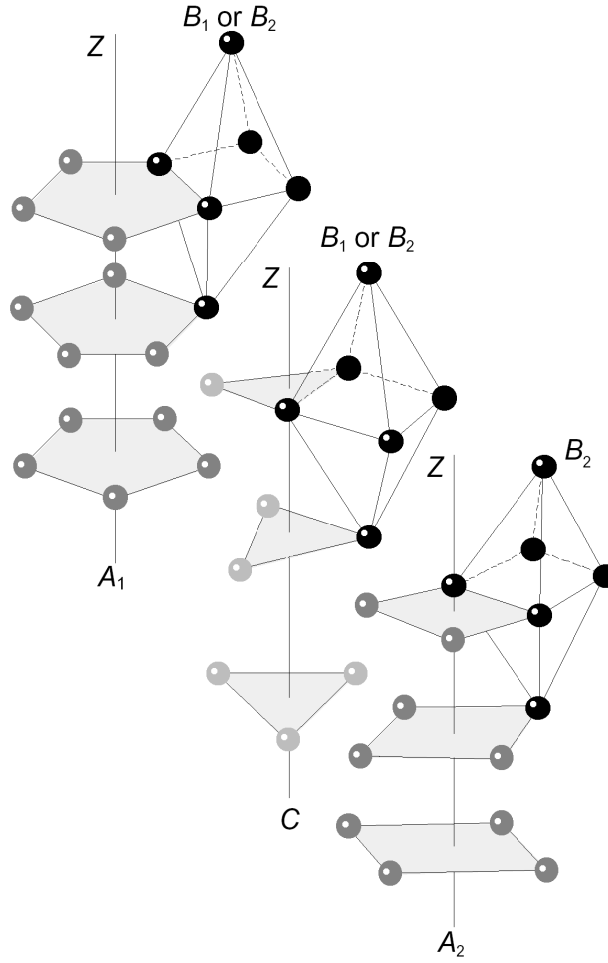


Figure 2.2: Detailed view of the structural. channels in SBN crystal. [13]

## 2.2 Optical Properties

The optical properties of solids provide an important tool for studying energy band structure, impurity levels, excitons, localized defects, lattice vibrations, and certain magnetic excitations. In such experiments, some observable are measured, such as reflectivity, transmission, absorption or light scattering.

### 2.2.1 Interband Transitions and Band Edge Absorption

The band gap is the energy difference between the top of the valence band and the bottom of the conduction band. The photon energy increases and becomes comparable to the energy gap, a new conduction process can occur. A photon can excite an electron from an occupied state in the valence band to an unoccupied state in the conduction band. This is



called an interband transition and is represented schematically by the picture in Fig. 2.3. In this process the photon is absorbed, an excited electronic state is formed and a hole is left behind. The interband transitions have a threshold energy at the energy gap. That is

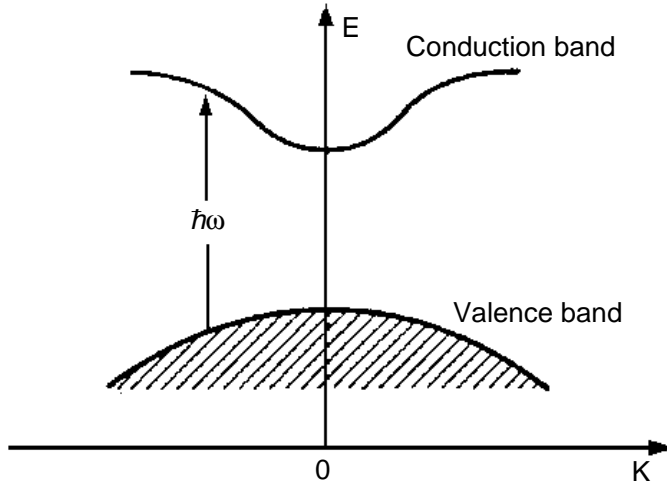


Figure 2.3: Schematic diagram of an allowed interband transition.

shown in Fig. 2.4.

The transitions are either direct (conserve crystal momentum  $\mathbf{k}$ :  $E_v(\mathbf{k}) \rightarrow E_c(\mathbf{k})$ ) or indirect (a phonon is involved because the  $\mathbf{k}$  vectors for the valence and conduction bands differ by the phonon wave vector  $\mathbf{q}$ ). Conservation of crystal momentum yields  $\mathbf{k}_{valence} = \mathbf{k}_{conduction} \pm \mathbf{q}_{phonon}$ . In discussing the direct transitions, one might wonder about conservation of crystal momentum with regard to the photon. For a typical optical wavelength of  $6000 \text{ \AA}$ , the wave vector for the photon is  $K = 2\pi/\lambda = 10^5 \text{ cm}^{-1}$ , while a typical size of the Brillouin zone is  $10^8 \text{ cm}^{-1}$ . Thus, typical direct optical interband processes excite an electron from a valence to a conduction band without a significant change in the wave vector.

### The Absorption Coefficient

The measurement of the absorption of light is one of the most important techniques for optical measurements in solids. In the absorption measurements, it is important to know the light intensity  $I(z)$  after a traversal of a thickness  $z$  of material as compared with the incident intensity  $I_0$ , thereby defining the absorption coefficient  $\alpha_{abs}(\omega)$ :

$$I(z) = I_0 e^{-\alpha_{abs}(\omega)z} \quad (2.1)$$

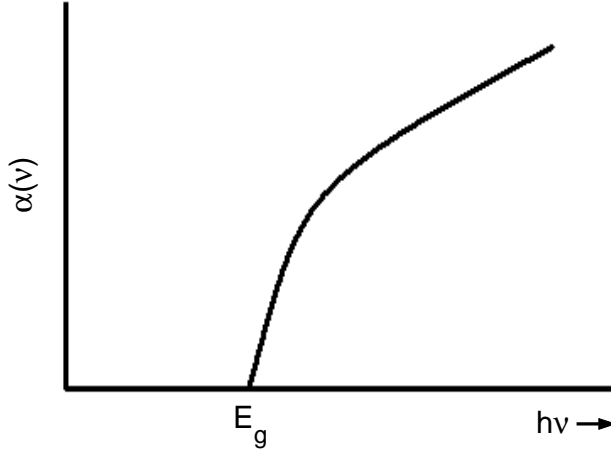


Figure 2.4: Frequency dependence of the absorption coefficient near a threshold for inter-band transitions.

where the behavior of the absorption constant is shown schematically in Fig. 2.4. Since the intensity  $I(z)$  depends on the square of the field variables, it immediately follows that

$$\alpha_{abs}(\nu) = 2 \frac{\omega \tilde{\kappa}(\omega)}{c} \quad (2.2)$$

where the factor of 2 results from the definition of  $\alpha_{abs}(\omega)$  in terms of the light intensity, which is proportional to the square of the fields. This expression tells us that the absorption coefficient is proportional to  $\tilde{\kappa}(\omega)$ , the imaginary part of the complex index of refraction (extinction coefficient), so that  $\kappa$  is usually associated with power loss.

The shape of the absorption edge immediately above  $E_g$  is calculated to vary as  $(\hbar\omega - E_g)^{1/2}$  for allowed direct transitions and as  $(\hbar\omega - E_g)^{3/2}$  for forbidden direct transitions. For indirect transitions the calculated shape is  $(\hbar\omega - E_g \pm \hbar\omega_p)^2$ , involving the temperature dependence of phonon populations.

### 2.2.2 Vibrational Transitions and Infrared Absorption

The energy  $E_p$  of a photon is equal to  $h\nu_p$  where  $\nu_p$  is its frequency. Under certain circumstances an unsymmetrical diatomic molecule can increase its vibrational energy by an amount  $\Delta E_m$  by absorbing the energy of a photon  $E_p$

$$\Delta E_m = E_p = h\nu_p \quad (2.3)$$

The only variable in the vibrational energy equation  $E_m = (n + \frac{1}{2})h\nu_m$  is the quantum number  $n$ . If the quantum number changes by +1 then the diatomic molecule gains energy by an amount  $\Delta E_m$  equal to the above energy equation subtracted from the same equation where  $n + 1$  is substituted for  $n$ .

$$\Delta E_m = \left[ (n + 1) + \frac{1}{2} \right] h\nu_m - \left( n + \frac{1}{2} \right) h\nu_m$$

so

$$\Delta E_m = h\nu_m \quad (2.4)$$

By combining Eqs. 2.3 and 2.4 it is clear that

$$\nu_p = \nu_m \quad (2.5)$$

The photon which has the appropriate energy to increase the vibrational quantum number by one has a frequency equal to the classical vibrational frequency of the molecule. If the quantum number should change by -1 then  $\Delta E_m = -h\nu_m$  and the molecule loses energy. In this case a photon with the same frequency will be emitted by the molecule to maintain the energy balance. In the quantum mechanical harmonic oscillator the vibrational quantum number can change only by  $\pm 1$ . All other transitions are forbidden if the vibration is harmonic. This quantum mechanical selection rule corresponds to the classical picture where the vibrational energy can be changed only when the electric field of the photon and dipole moment of the molecule vibrates with the same frequency.

If the quantum number changes by +2 then

$$\Delta E_m = \left[ (n + 2) + \frac{1}{2} \right] h\nu_m - \left( n + \frac{1}{2} \right) h\nu_m; \quad \Delta E_m = 2h\nu_m \quad (2.6)$$

When Eq. 2.6 is combined with Eq. 2.3 we obtain

$$\nu_p = 2\nu_m \quad (2.7)$$

so that the photon which has the right energy to increase the quantum number by two has a frequency twice that of the molecule. If the vibration is harmonic there is no dipole moment component vibrating at this frequency so there is no way to induce this transition. If the vibration is anharmonic there will be a small dipole moment component vibrating at 2, 3, 4, etc., times the molecular frequency. This corresponds to the selection rule where in an anharmonic quantum mechanical oscillator the quantum number may change by  $\pm 1$ ,  $\pm 2$ ,  $\pm 3$ , ...

The harmonic oscillator approximation is adequate for most of the features of the spectrum, but some of the finer details such as the appearance of overtones indicate that real molecules have somewhat anharmonic potential functions. A typical anharmonic potential for which the Schrödinger equation has an exact solution is the Morse-potential

$$U(r - r_e) = D_e[1 - \exp(-\beta(r - r_e))]^2 \quad (2.8)$$

where  $r_e$  is the equilibrium distance of the two vibrating atoms,  $D_e$  (the binding energy) and  $\beta$  are constants. A quantum mechanical treatment of the anharmonic oscillator yields the following equation for the energy levels.

$$E_{vib} = hc\bar{\nu}_e \left(n + \frac{1}{2}\right) - hc x_e \bar{\nu}_e \left(n + \frac{1}{2}\right)^2 + \dots \quad (2.9)$$

Higher order terms are usually not needed. The energy level terms expressed in  $\text{cm}^{-1}$  ( $E/hc$ ) are given by

$$\frac{E_{vib}}{hc} = \bar{\nu}_e \left(n + \frac{1}{2}\right) - x_e \bar{\nu}_e \left(n + \frac{1}{2}\right)^2 \dots \quad (2.10)$$

Unlike the harmonic oscillator energy levels, these are no longer equally spaced. One result is that hot bands ( $n = 2 \leftarrow n = 1$ , etc.) will no longer have exactly the same frequency as the fundamental ( $n = 1 \leftarrow n = 0$ ) band. This result corresponds to the classical case where the frequency is no longer completely independent of the amplitude when mechanical anharmonicity is present.

As was stated before, overtone transitions such as  $n = 0$  to  $n = 2, 3, 4, \dots$ , are allowed in an anharmonic oscillator. However, the nonuniform spacing of the energy levels in

an anharmonic oscillator means that an overtone will not be found at exactly 2, 3, 4,..., times the frequency of the fundamental. The wavenumber  $\bar{\nu}_n$  of the fundamental and its overtones are given by subtracting from Eq. 2.10, the same equation with  $n = 0$ , and setting  $\Delta E_{vib}/hc = \bar{\nu}_n$

$$\bar{\nu}_n \equiv n\bar{\nu}_e(1 - x_e(n + 1)) \quad n = 1, 2, 3, \dots \quad (2.11)$$

Thus from the wavenumber of the fundamental ( $\bar{\nu}_1$ ) and the first overtone ( $\bar{\nu}_2$ ) one can calculate  $x_e$ ,  $\bar{\nu}_e$  and the Morse-potential parameter  $\beta$  and  $D_e$ .

### 2.2.3 The Raman Effect

In a Raman spectrometer the sample is irradiated with an intense source of monochromatic radiation. Usually this radiation frequency is much higher than the vibrational frequencies but is lower than electronic frequencies.

The Raman effect can be looked on as an inelastic collision between the incident photon and the molecule where as a result of the collision the vibrational or rotational energy of the molecule is changed by an amount  $\Delta E_m$ . In order that energy may be conserved, the energy of the scattered photon,  $h\nu_s$ , must be different from the energy of the incident photon  $h\nu_i$ , by an amount equal to  $\Delta E_m$

$$h\nu_i - h\nu_s = \Delta E_m \quad (2.12)$$

If the molecule gains energy then  $\Delta E_m$  is positive and  $\nu_s$  is smaller than  $\nu_i$ , giving rise to Stokes lines in the Raman spectrum. If the molecule loses energy, then  $\Delta E_m$  is negative and  $\nu_s$  is larger than  $\nu_i$ , giving rise to anti-Stokes lines in the Raman spectrum.

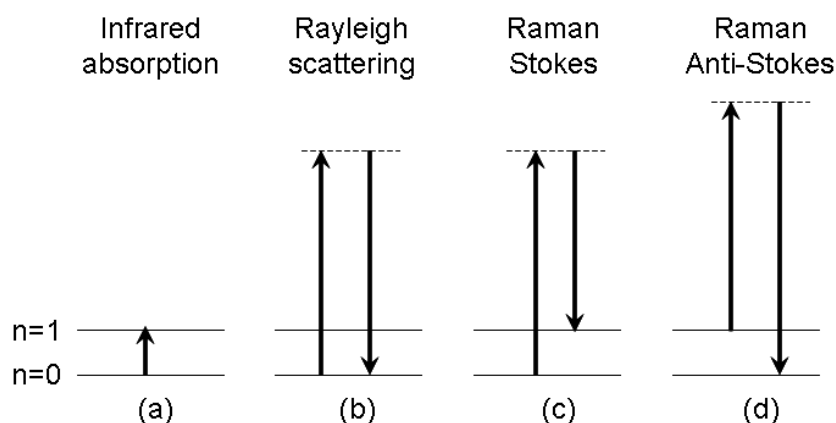


Figure 2.5: Schematic illustration of Raman and Rayleigh scattering and infrared absorption. In infrared absorption the incident photon has the same frequency as the molecular vibration. In Raman and Rayleigh scattering the incident photon has a much higher frequency.

### Fundamentals of Raman Scattering

In order for a molecular vibration to be Raman active, the vibration must be accompanied by a change of the polarizability of the molecule. We consider a two-atom molecule. For

an applied field  $E(\nu)$  the polarizability  $\alpha_0$  of the orbitals shown leads to a dipole moment

$$P_D(\nu) = \alpha_0 E(\nu) \quad (2.13)$$

If the molecule is vibrating with frequency  $\nu_v$ , a change in the polarizability results. For small displacements the polarizability can be expanded in a Taylor serie as

$$\alpha = \alpha_0 + \frac{\partial \alpha}{\partial Q} Q + \dots \quad (2.14)$$

where  $\alpha_0$  is the equilibrium polarizability,  $Q$  is a normal coordinate, while varied periodically.

In this case the total dipole moment has the form

$$P_D(\nu) = \left( \alpha_0 + \frac{\partial \alpha}{\partial Q} Q_0 \cos 2\pi \nu_v t \right) E_0 \cos 2\pi \nu t \quad (2.15)$$

Application of trigonometric sum rules yields

$$P_D(\nu) = \alpha_0 E_0 \cos 2\pi \nu t + \frac{\partial \alpha}{\partial Q} \frac{Q_0 E_0}{2} [\cos 2\pi(\nu + \nu_v)t + \cos 2\pi(\nu - \nu_v)t] \quad (2.16)$$

It can be seen from this equation that the induced dipole moment  $P_D$  varies with three frequencies  $\nu_v$ ,  $\nu - \nu_v$  and  $\nu + \nu_v$  and can therefore give rise to Rayleigh scattering, Stokes and anti-Stokes Raman scattering, respectively.

In crystals the situation is more complicated since the phonons have periodic structures and scattering from different parts of the wave will interfere. A constructive interference occurs for the condition

$$2\Lambda \sin(\theta/2) = n\lambda \quad (2.17)$$

$\Lambda$  and  $\lambda$  are the wavelengths of the phonon and of the light, respectively,  $n$  is the index of refraction, and  $\theta$  the angle between the incident and the scattered beam. Equation 2.17 means that scattering occurs in a well defined direction for a given phonon and for a given wavelength of the incident light.

From classical theory it is known that the intensity of scattered radiation is proportional to the fourth power of the frequency and to the square of the maximum value of the excitation electric field ( $E_0^2$ ). The intensity of Rayleigh scattered radiation is proportional to  $\alpha_0^2$  and the intensity of Raman scattered radiation is proportional to  $(\partial \alpha / \partial Q)^2$ . The

main deficiency of the classical treatment of the Raman effect is that it predicts an incorrect value for the intensity ratio of anti-Stokes to Stokes bands. The correct ratio is

$$\frac{\text{anti - Stokes intensity}}{\text{Stokes intensity}} = \frac{(\nu + \nu_v)^4}{(\nu - \nu_v)^4} e^{-(h\nu_v/KT)} \quad (2.18)$$

In the classical treatment the exponential term is not present.

### Raman Tensor

For a description of the Raman scattering process and for a evaluation of the Raman intensity we can proceed analogous to 2.15. Instead of the scalar polarizability  $\alpha$  we use the susceptibility tensor  $\chi_{jl}$  in the case of the crystals. The displacements of the atoms are replaced by the normal coordinates  $Q_k$  of the oscillations. The susceptibility can then be expanded with respect to the normal coordinates  $Q_k$  and one obtains in analogy to  $\alpha$  in 2.15

$$\chi_{jl} = (\chi_{jl})_0 + \sum_k \left( \frac{\partial \chi_{jl}}{\partial Q_k} \right) + \dots \quad (2.19)$$

where the sum runs over all normal coordinates.  $\partial \chi_{jl} / \partial Q_k$  is a component of the derived polarizability tensor. This tensor is also know as the Raman tensor  $\chi_{jl,k}$ .

The intensity of the scattered light is proportional to the square of the Raman tensor.

$$I \propto \left| \sum_{j,l} e_j^s \cdot \chi_{jl,k} \cdot e_l^i \right|^2 \quad (2.20)$$

where  $e_j^i$  and  $e_l^s$  are the orientations of the polarizations of the incident and scattering light beams, respectively.

The components of the tensor have three indices.  $j$  and  $l$  extend over the coordinates 1 to 3 and  $k$  runs over the  $3N - 3$  normal coordinates for the vibrations, where  $N$  is the number of atoms in the unit cell. In other words,  $k$  runs over all optical modes with wave vector  $q = 0$ . Group theory enables the determination of which vibrational species can have non-vanishing components in their Raman tensor. Since the Raman intensities are described by symmetric tensors exactly those species are Raman active for which the representations are contained in the representation for the symmetric tensors. Group theory can predict even more. It determines which components of the Raman tensors must be zero in the various point group and which are finite. Thus, the structure of the Raman tensors can



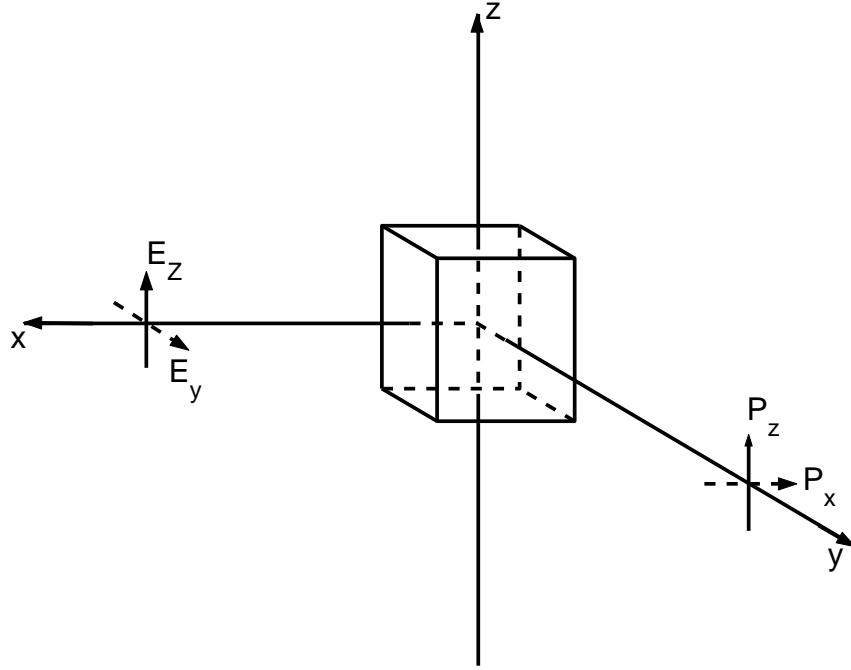


Figure 2.6: Beam and sample geometry for  $90^\circ$  scattering.

be evaluated for all vibrational species and for all point groups. The tensors are tabulated in many books. For example, the Raman tensor for a tetragonal point group  $C_{4v}$  has the form

$$(\chi)_{A_1} = \begin{pmatrix} a & 0 & 0 \\ 0 & a & 0 \\ 0 & 0 & b \end{pmatrix} \quad (2.21)$$

For the characterization of the scattering geometry the directions of the incident and scattered light as well as the directions of the corresponding polarizations are important. It is convenient to describe these directions with the symbol  $a(bc)d$ , where the letters usually refer to Cartesian coordinates  $x$ ,  $y$  and  $z$ . The parameters  $a$  and  $d$  give the directions for the incident and scattered light, and  $b$  and  $c$  the directions for the corresponding polarizations. This assignment is known as Porto notation. The Porto notation for the scattering geometry of the solid arrows in Fig. 2.6 is  $X(ZZ)Y$ .

## 2.3 Dielectric Properties

### 2.3.1 Polarization, Pyroelectricity

There are 32 point groups, 21 out of them are non-centrosymmetric and 20 of these exhibit piezoelectricity. A further sub-division can be made and consists of point groups which have a unique polar axis. Such materials, when heated, exhibit the phenomenon known as pyroelectricity, which can be defined as the ability of a material to generate a charge when being uniformly heated.

All ferroelectric materials are pyroelectric since they have a unique polar axis. The definition of a ferroelectric requires that the dipole must be reversible under an applied field.

When an electric field is applied to a polar material, the total dielectric displacements,  $\mathbf{D}$ , the magnitude of which is equal to the charge density, is given by:

$$\mathbf{D} = \varepsilon_0 \mathbf{E} + \mathbf{P}_{total} = \varepsilon_0 \mathbf{E} + (\mathbf{P}_s + \mathbf{P}_{ind}) \quad (2.22)$$

where  $\varepsilon_0$  is the permittivity of free space,  $\mathbf{E}$  is the applied field,  $\mathbf{P}_s$  and  $\mathbf{P}_{ind}$  are the spontaneous and induced components of polarization, respectively. The permittivity of a material is defined as:

$$\varepsilon = \varepsilon_0(1 + \chi_e) \quad (2.23)$$

where  $\chi_e$  is the electric susceptibility ( $\chi_e = \varepsilon_r - 1$ ). In general,  $\chi_e$  is a second-rank tensor; however, if  $\mathbf{P}$  and  $\mathbf{E}$  are parallel, then  $\chi_e$  reduces to a scalar. For a linear dielectric:

$$\mathbf{P}_{ind} = \chi_e \varepsilon_0 \mathbf{E} \quad (2.24)$$

and  $\mathbf{D}$  can therefore be re-written as:

$$\mathbf{D} = \varepsilon \mathbf{E} + \mathbf{P}_s \quad (2.25)$$

The partial derivative (assuming constant  $\mathbf{E}$ ) of this equation with respect to the temperature yields the generalized pyroelectric coefficient:

$$\frac{\partial \mathbf{D}}{\partial T} = \frac{\partial \mathbf{P}_s}{\partial T} + \mathbf{E} \frac{\partial \varepsilon}{\partial T} \quad (2.26)$$

or

$$\mathbf{p}_g = \mathbf{p} + \mathbf{E} \frac{\partial \varepsilon}{\partial T} \quad (2.27)$$

where  $\mathbf{p}_g$  is the generalized pyroelectric coefficient and  $\mathbf{p} = \partial \mathbf{P}_s / \partial T$  is the true pyroelectric coefficient, as it reflects the change in spontaneous polarization as a function of temperature. The general coefficient,  $\mathbf{p}_g$ , assumes the presence of an applied field  $\mathbf{E}$ . The  $\mathbf{E} \partial \epsilon / \partial T$  term applies to all dielectrics, whether polar or not; but as the temperature coefficient of the permittivity is always high in ferroelectrics, in this case the effect can be comparable in size to the true pyroelectric effect.

# Chapter 3

## Optical Properties

### 3.1 Band Edge Absorption

#### 3.1.1 Experimental Method, Omega 10 Spectrophotometer

In this measurement we used c-cut and a-cut thin plates (thickness 0.5 mm) of  $\text{Sr}_x\text{Ba}_{1-x}\text{Nb}_2\text{O}_6$  crystals with the composition varying from  $x = 0.32$  to  $x = 0.79$ . The crystals were polished to optical quality. The absorption was measured with an Omega 10 spectrophotometer (Bruins Instruments) with an accuracy of 0.1 nm after calibration with a mercury lamp.

We made two kind of measurements. In one we measured the band edge energy as a function of the composition. In this measurement we used c-cut samples for measuring the ordinary light polarization and a-cut samples for both ordinary and extra-ordinary light polarization. All measurements were carried out at room temperature ( $T = 22^\circ\text{C}$ ). For the second measurement we used five a-cut crystals and measured the temperature dependence of the band edge energy for both ordinary and extra-ordinary light polarization. In this measurement the temperature was varied between 50 and 400 K in a gas flow cryostat, with a temperature stability of 2 K.

The Omega spectrophotometer is a computer controlled double-beam spectrophotometer for the UV, visible and NIR. This instrument combines high optical resolution with a very fast scan speed.

Fig. 3.1 shows the scheme of the Omega 10 spectrophotometer. The component parts of the spectrophotometer are:

- light source - two lamps (halogen lamp and deuterium lamp). For scans in the UV

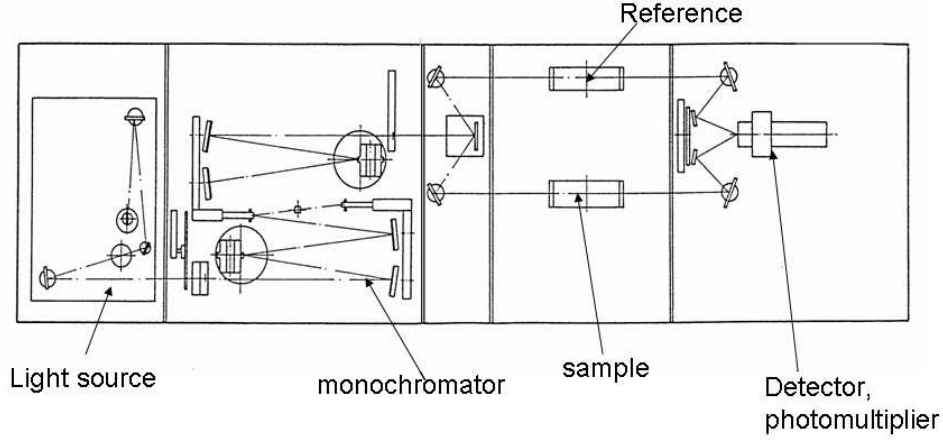


Figure 3.1: Omega 10 spectrophotometer.

it is necessary to have the deuterium lamp switched on.

- filters and attenuators
- slit
- double monochromator
- beam switch - switches the beam between reference and sample channel
- sample holder
- optical detector.

### 3.1.2 Results and Discussion

The absorption data have been corrected for reflection losses, applying standard equations Eq. 3.1 (*multiple pass reflection correction*) [21].

$$\alpha = -\frac{1}{d} \ln \left( -g + \sqrt{g^2 + \frac{1}{R^2}} \right), \quad g = \frac{(1 - R)^2}{2TR^2} \quad (3.1)$$

where  $\alpha$  is the absorption coefficient,  $d$  the thickness of the sample along the light propagation direction,  $T = I/I_o$  the transmission and  $R = (n - 1)^2/(n + 1)^2$  with  $n$  denoting the refractive index. The values of the index of refraction were measured by A. Tunyagi,

using the minimum deviation method. A global fit was made over the whole composition range using a four-parameter Sellmeier equation Eq. 3.2. A good fit can be achieved assuming that all coefficients of this equation are linear functions of the composition  $x$  for the extraordinary refractive indices ( $n_e$ ) and constant for ordinary refractive indices ( $n_o$ ).

$$n^2(\lambda) = A + \frac{B}{\lambda^2 - C} + D\lambda \quad (3.2)$$

Figure 3.2 shows the absorption spectra of one SBN crystal for ordinary and extra-ordinary light polarization at room temperature. In this case the difference of the band edge energy at an absorption value of  $\alpha = 100 \text{ cm}^{-1}$  between the ordinary and extra-ordinary light polarization is approximative 0.06 eV.

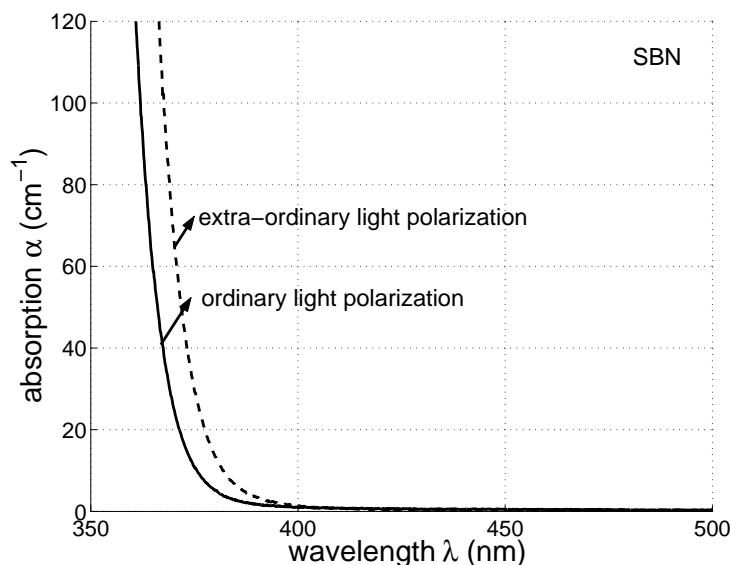


Figure 3.2: Absorption spectra of SBN for ordinary and extra-ordinary light polarization.

The knowledge of the band edge (energy or wavelength corresponding to a certain absorption coefficient) for polarized light absorption as a function of composition is useful for a nondestructive determination of the composition of a crystal.

In the  $\text{LiTaO}_3$  crystals we have a large and monotonic shift of the band edge as a function of the composition [22].

In many solid solutions the properties change with composition in a linear manner according to Vegards rule, the value of a property is linearly interpolated from the endpoint of the composition range. Often the lattice constants follow this rule, but for other parameters

like the band edge energy a second order model is needed. Therefore a description according to

$$E_g(x) = E_g^A (1 - x) + E_g^B x - b x (1 - x) \quad (3.3)$$

is often introduced, where  $(E_g^A, E_g^B)$  are the band gap energies of the subsystems and  $b$ , characterizing the deviation from linearity, is called the bowing parameter. Several band structure models have been proposed to predict the value of  $b$ . Most of these models describe  $b$  adequately but differ particularly in how the effect of disorder of different cations (anions) is treated in the band structure [23]. Theoretical studies have been hampered by the problems of incorporating inhomogeneities into periodic crystals. The virtual-crystal approximation is one approach to overcome these difficulties. Using this method a composite potential is constructed which represents the average of the component atoms comprising the inhomogeneity. Already in 1983 A. Zunger and J. E. Jaffe [24] pointed out that often the anion-cation bond lengths do not average to a single bond but instead remain close, throughout the composition range, to their respective values in the endpoints. To gain more insight into the physics Bernard and Zunger [25] proposed a decomposition of the bowing parameter into physically distinct contributions like the volume deformation, the charge exchange and the structural relaxation. We are not aware of any calculation of the bowing parameter in SBN, therefore we present the parameters (Table: 3.1) but are unable to perform a conclusive decomposition.

	$E_g^A$ (eV)	$E_g^B$ (eV)	$b$ (eV)
(o)-pol. light	3.494	3.451	0.207
(eo)-pol. light	3.466	3.411	0.296

Table 3.1: Fit parameters for the composition dependence of the band edge.

In the case of SBN crystals (see the Fig. 3.3) the shift of the band edge is weak ( $< 0.02$  eV) and not monotonic. It has a minimum for both light polarizations close to the congruently melting composition. Also, the bowing parameter  $b$  is quite small compared to values obtained in semiconductors (as large as 10 eV).

In the second part we will discuss the temperature dependence of the band edge of SBN with different Sr content. This has been reported in [26, 27, 28] for the congruent composition of SBN. In Fig. 3.4 we plotted the temperature dependence of the energy at an absorption value of  $\alpha = 100 \text{ cm}^{-1}$  for SBN with  $x=0.689$  for ordinary and extraordinary

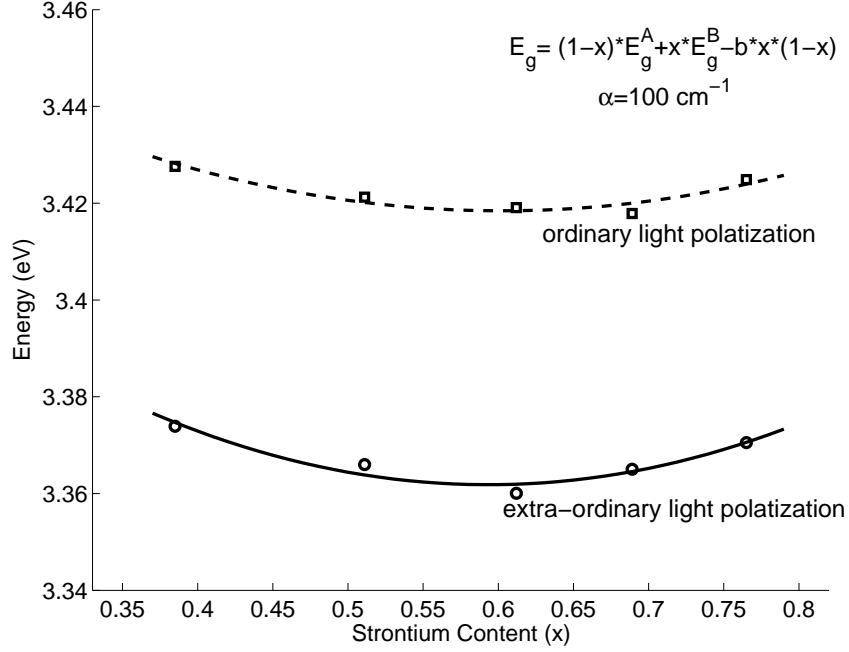


Figure 3.3: Composition dependence of the band edge in SBN taken at an absorption value of  $\alpha = 100 \text{ cm}^{-1}$  for ordinary and extra-ordinary light polarization.

light polarization and the difference of the band edge energies for ordinary and extra-ordinary light polarization. The plotting was done only for a single composition of a SBN crystal, because for all the other compositions the temperature dependence of the band edge has the same behavior. It is possible to observe from Fig. 3.4 that for a temperature higher than  $T = 200 \text{ K}$  there exists a linear dependence which turns into a flat part for  $T$  below  $100 \text{ K}$ . We did not notice any peculiarities of the absorption in the phase transition region.

The band edge temperature expression  $E_g(T)$  have the general form  $E_g^0 - KN$ , where  $K$  describes the electron-lattice coupling and  $N$  the occupation number. Expressions of the occupation number  $N$  are usually based on the Bose-Einstein statistics. For describing the temperature dependence of the band edge it is sufficient to use a single Einstein oscillator because the internal energy of a set of optical phonon modes having different energies is very closely equal to the internal energy of a single phonon system with an energy being the average of the multi-phonon set [29].

For fitting of the date we adopted the expression from the articles [28, 30].



$$E_g(T) = E_g(0) - \beta k\Theta \left( \frac{1}{\exp(\Theta/T) - 1} \right) \quad (3.4)$$

$E_g(0)$  is the energy at  $T = 0$ ,  $\beta$  is a dimensionless coupling constant describing the slope of  $E_g$  for high temperatures ( $T \rightarrow \infty$ ), while  $k\Theta$  is an averaged phonon energy.

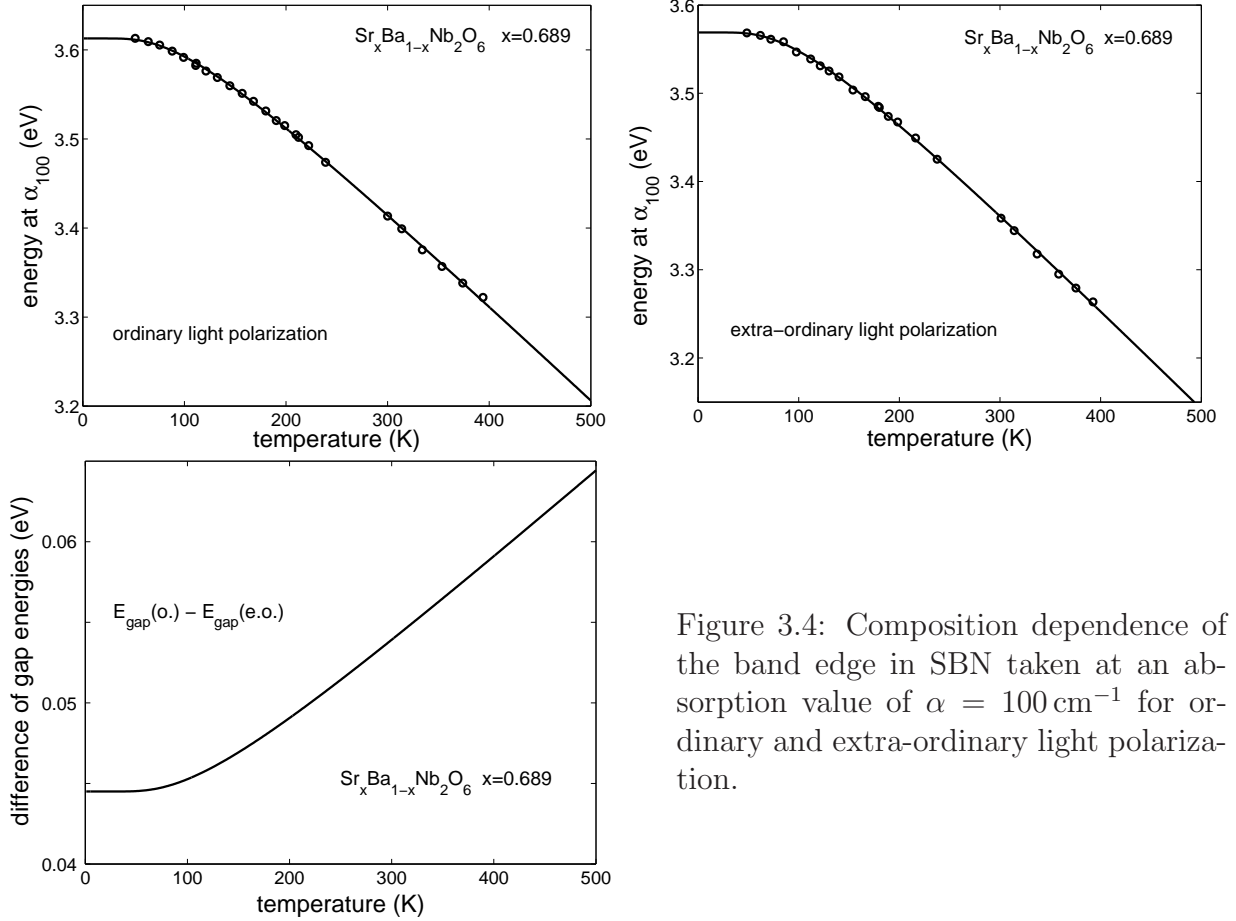


Figure 3.4: Composition dependence of the band edge in SBN taken at an absorption value of  $\alpha = 100 \text{ cm}^{-1}$  for ordinary and extra-ordinary light polarization.

In conclusion, we want to mention that for our fits we used the one oscillator model (like by Meyer et al. [28]). In this case we obtain the maximum slope  $\beta k = -1.3 \text{ meV/K}$  for the congruent SBN crystal, in agreement with the experimental fitting in [27, 28] and the slope decreases at  $-1 \text{ meV/K}$  for the Ba and Sr rich sizes.

From Tab. 3.2 we conclude that the parameter  $E_g(0)$  reflects the band bowing while  $\beta$  and  $\theta$  are almost constant if we neglect the values for the congruent composition. The origin for this scatter is unknown.

	x	$E_g(0)$ (eV)	$\beta$	$\Theta$ (K)
(o)-pol. light	0.342	3.6218	12.3069	297.7977
	0.477	3.6094	12.1911	288.4730
	0.612	3.6027	14.9093	404.3301
	0.689	3.6112	12.6194	280.6127
	0.765	3.6190	11.7866	261.5971
(eo)-pol. light	0.342	3.5918	12.9588	255.0042
	0.477	3.5761	12.9504	255.4589
	0.612	3.5675	14.8303	345.5590
	0.689	3.5667	13.3116	284.3174
	0.765	3.5745	12.1368	252.2834

Table 3.2: Fit parameters for the temperature dependence of the band edge.

## 3.2 OH<sup>-</sup> stretching vibration

The aim of the experiment is to investigate the shape of the OH<sup>-</sup> band in Sr<sub>x</sub>Ba<sub>1-x</sub>Nb<sub>2</sub>O<sub>6</sub> crystals in a wide composition range ( $x = 0.38$  to  $0.79$ ) in order to obtain more information about the relation between the band components and the crystal structure, as well as the occupancy of the proton sites and the cation distribution in the structural channels.

Hydroxyl ions are often present in as-grown oxide crystals [31]. Their stretching vibrational mode can easily be detected by infrared (IR) absorption spectroscopy. As-grown SBN crystals studied so far contained only a small amount of hydroxyl ions, probably as a result of the humid atmosphere during the growth process. To allow a conclusive analysis of the OH<sup>-</sup> spectral band shape we raised the hydroxyl ion concentration of the as-grown crystals by about one order of magnitude modifying some well-known treatments [32, 33].

### 3.2.1 FT-IR Spectrometer

A Fourier-Transform-Infrared Spectrometer ( FT-IR ) is typically based on a Michelson Interferometer; an example is shown in Fig. 3.5. The interferometer consists of a beam splitter, a fixed mirror, and a mirror that translates very precisely back and forth. The beam splitter is made of a special material that transmits half of the radiation striking it and reflects the other half. Radiation from the light source strikes the beam splitter and separates into two beams. One beam is transmitted through the beam splitter to the fixed mirror and the second is reflected off the beam splitter to the moving mirror. The

fixed and moving mirrors reflect the radiation back to the beamsplitter. Again, half of this reflected radiation is transmitted and half is reflected at the beam splitter, resulting in one beam passing to the detector and the second back to the source. If the two beams are

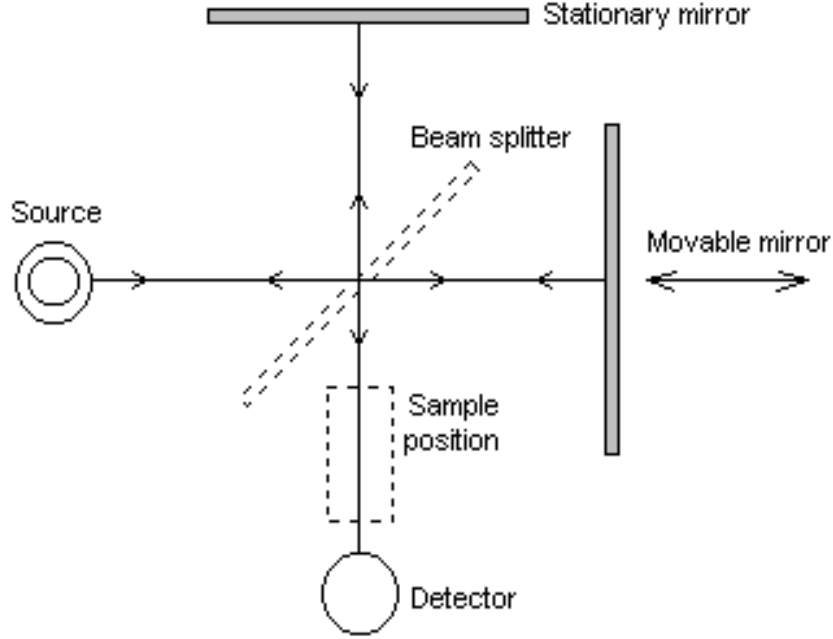


Figure 3.5: The Michelson interferometer.

monochromatic light with the same amplitude  $a_0$ , the amplitude of the interference light is

$$\begin{aligned} a(x, t) &= a_0(e^{i\omega t} + e^{i(\omega t + 2\pi\bar{\nu}_0 x)}) \\ &= 2\cos(\pi\bar{\nu}_0 x) e^{i(\omega t + \pi\bar{\nu}_0 x)} \end{aligned} \quad (3.5)$$

where  $x$  is the optical path difference of the two beams. The intensity  $\tilde{I} = aa^*$  is given by

$$\tilde{I}(x) = 4\tilde{I}_0 \cos^2(\pi\bar{\nu}_0 x) = 2\tilde{I}_0(1 + \cos(2\pi\bar{\nu}_0 x)) \quad \text{with} \quad \tilde{I}_0 = a_0 a_0^* \quad (3.6)$$

For all wavenumbers  $\bar{\nu}$  ( $0 < \bar{\nu} < \infty$ ) we obtain

$$I(x) = \int_0^\infty 2\tilde{I}(\bar{\nu}) d\bar{\nu} + \int_0^\infty 2\tilde{I}(\bar{\nu}) \cos(2\pi\bar{\nu}x) d\bar{\nu} \quad (3.7)$$

because

$$I(0) = 4 \int_0^\infty \tilde{I}(\bar{\nu}) d\bar{\nu} \Rightarrow \int_0^\infty 2\tilde{I}(\bar{\nu}) d\bar{\nu} = \frac{1}{2}I(0) \quad (3.8)$$

Therefore the interferogram function is written as

$$I_i(x) = I(x) - \frac{1}{2}I(0) = \int_{-\infty}^\infty I(\bar{\nu}) \cos(2\pi\bar{\nu}x) d\bar{\nu} \quad (3.9)$$

This is the intensity function as a function of the optical path difference  $x$ . With the Fourier transformation, we can calculate the intensity as a function of the wavenumber  $\bar{\nu}$

$$I_i(\bar{\nu}) = \int_{-\infty}^\infty I(x) \cos(2\pi\bar{\nu}x) dx \quad (3.10)$$

If the sample is placed behind the interferometer, the light intensity  $I_f(\bar{\nu})$  after transmitting the sample is given by the Lambert-Beer formula

$$I_f(\bar{\nu}) = I_i(\bar{\nu}) \exp(-\alpha d) \quad (3.11)$$

where  $I_i(\bar{\nu})$  is the light intensity before transmitting the sample,  $\alpha$  the absorption coefficient and  $d$  the thickness of the sample. Thus

$$\alpha = \frac{1}{d} \ln \frac{I_i(\bar{\nu})}{I_f(\bar{\nu})} \quad (3.12)$$

All the OH<sup>-</sup> absorption spectra were measured with a Fourier spectrometer (IFS120HR, Bruker). Fig. 3.6 illustrates the layout of this spectrometer. For different spectral ranges, different beamsplitters, detectors are required. Table 3.3 lists the combinations of the light sources, beamsplitters, detectors and the modulation frequencies for the measurements from UV to FIR spectral regions.

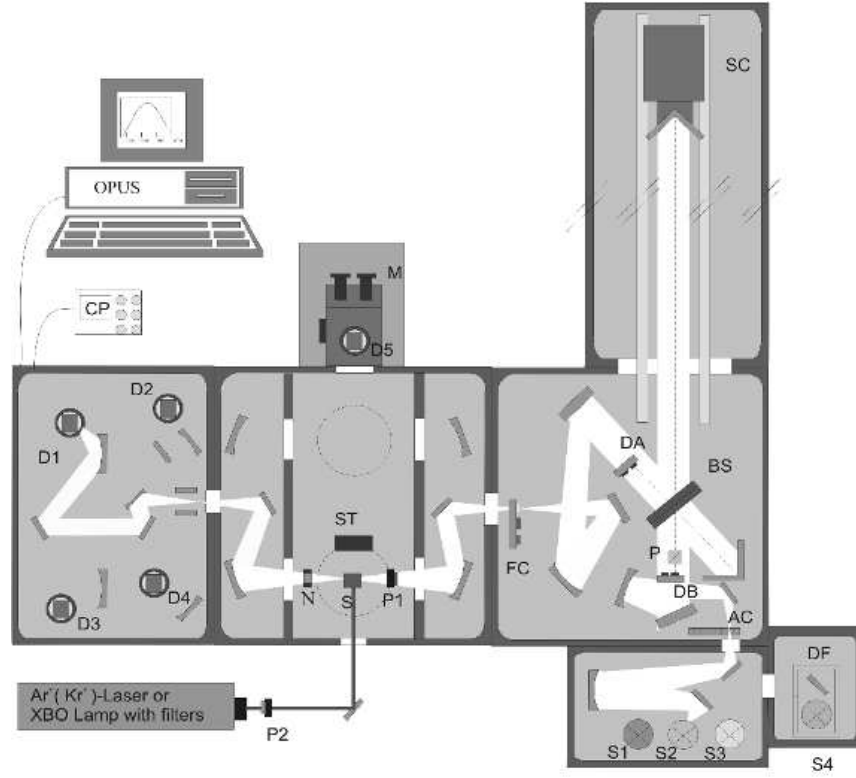
### 3.2.2 OH<sup>-</sup> doping

The Fig. 3.7 shows the scheme of the setup used for increasing the OH<sup>-</sup> content in crystals. For this treatment we put the sample into the quartz tube which is introduced into an oven. Inside the tube it is necessary to have a humid atmosphere. This humid atmosphere is obtained using air or oxygen flows through a water bottle held at an elevated temperature.

In the first step of the treatment we heat the sample at 800 °C for 10 h and wet vapor from

Range ( $\bar{\nu}$ in $\text{cm}^{-1}$ )	Source ( $\bar{\nu}$ in $\text{cm}^{-1}$ )	Beamsplitter ( $\bar{\nu}$ in $\text{cm}^{-1}$ )	Detector ( $\bar{\nu}$ in $\text{cm}^{-1}$ )	Modulation Frequency
UV (45,000-20,000)	Xenon (30,000-20,000)	UV/Quartz (45,000-8,000)	Photomultiplier (30,000-10,000) GaP-Diode (30,000-18,000)	5 (7.5 kHz) 5 (7.5 kHz)
VIS (20,000-10,000)	Tungsten (25,000-3,000)	VIS/Quartz (25,000-8,000)	Si-Diode (32,000-9,000)	7 (20 kHz)
NIR (10,000-2,000)	Tungsten (25,000-3,000)	Si/ $\text{CaF}_2$ (10,000-1,000)	Ge-Diode (14,000-6,500) $\text{LN}_2$ cooling  InSb (9,000-2,000) $\text{LN}_2$ cooling	4 (5 kHz)  8 (40 kHz)
FIR (2,000-100)	Globar (5,000-100)	Ge/KBr (4,800-400)	HgCdTe(MCT) (6,000-800) $\text{LN}_2$ cooling	6 (10 kHz)

Table 3.3: The light sources, beamsplitters, detectors and modulation frequencies for different spectra regions [34].



D1-D5	: Detectors;	S	: Sample;
S1-S4	: Light Sources;	P	: Coupling Prism;
M	: External Microscope;	SC	: Scanner;
DF	: Dichroic Filter;	DA-DB	: Diode Pairs;
FC	: Filter Changer;	OPUS	: Control Software;
AC	: Aperture Changer;	CP	: Control Panel;
ST	: Beam Stopper;	N	: Notchfilter;
P1-P2	: Polarizers;	BS	: Beam Splitter;

Figure 3.6: The Fourier spectrometer IFS120HR (Bruker) [34].

a water bottle held at 50 °C was flowing. In this situation the result was not promising, because the  $\text{OH}^-$  absorption intensity of the crystal is lower ( $\alpha = 0.25 \text{ cm}^{-1}$ ) than that reported in the literature [31]. If the temperature of the water was increased to 80 °C, the absorption coefficient was higher but not high enough. To increase the temperature of the water more is not a solution, because we did not obtain a higher value. Next we tried to increase the temperature of sample, but we observed a significant reduction of the crystal for temperatures higher than 800 °C. If we use instead of air pure oxygen it was possible to increase the temperature of the sample up to 900 °C without a significant reduction.

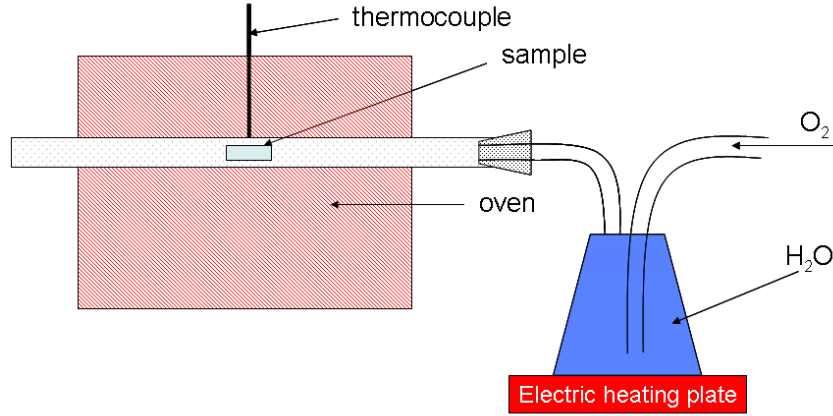


Figure 3.7: OH doping setup

Finally we treated all samples at  $900^\circ\text{C}$  for 10 h with wet oxygen, which flows through a water bottle held at  $80^\circ\text{C}$ . This method guaranteed a strong  $\text{OH}^-$  doping, but avoided significant reduction of the crystals resulting in disturbing polaron absorption.

### 3.2.3 Results, Data Fiting and Discussion

#### Results

Treating a dozen c-cut samples of different crystal compositions ( $0.38 < x < 0.79$ ) at  $900^\circ\text{C}$  for 10 h with wet oxygen yields a pronounced increase of the  $\text{OH}^-$  absorption depending on the composition. This doping at moderate temperature and pressure produces a composition dependent absorption coefficient of about  $0.3\text{--}1\text{ cm}^{-1}$  for the main band, which is comparable to other procedures [32]. In Fig. 3.8 we have shown the ordinarily polarized absorption of c-cut samples after background subtraction. The spectra were shifted vertically for better viewing.

It is evident from Fig. 3.8 that the intensity of the main band at about  $3493\text{ cm}^{-1}$  increases with  $x$ , and the shape is definitely influenced. The integral absorption being proportional to the  $\text{OH}^-$  ion content of the crystals increases in an almost linear manner as a function of  $x$ , see Fig. 3.9. Sr-rich samples accept approximately three times more hydrogen than Ba-rich ones when treated under equal conditions.

The  $\text{OH}^-$  spectra of congruent material taken with extraordinarily polarized light reported previously [32, 33] have shown a strongly reduced absorption. Moreover, the  $\text{OH}^-$  band for the ordinary polarization at  $3495\text{ cm}^{-1}$  disappeared and a higher frequency band emerged

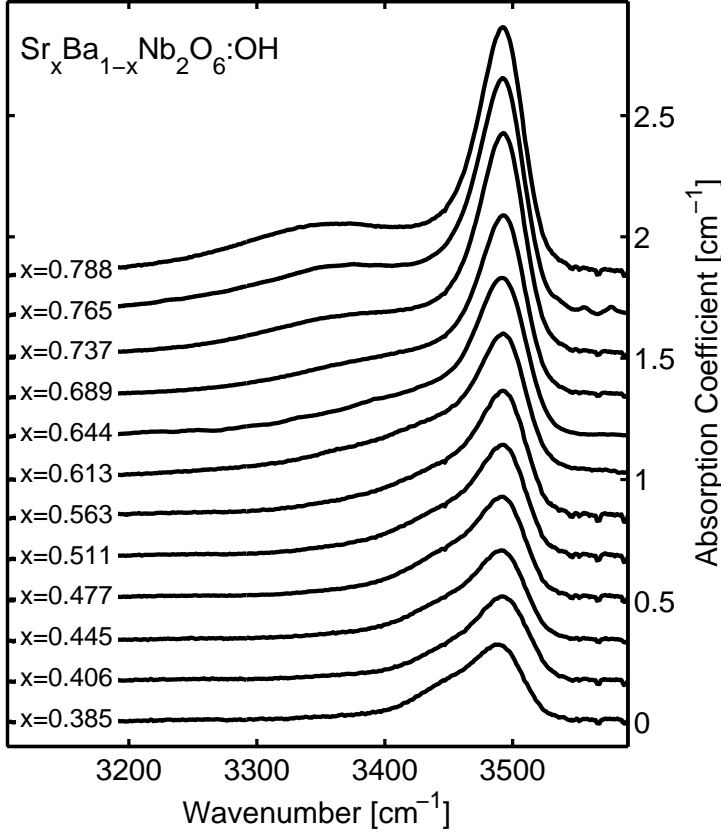


Figure 3.8: Absorption spectra of the  $\text{OH}^-$  stretch mode for various  $\text{Sr}_x\text{Ba}_{1-x}\text{Nb}_2\text{O}_6$  crystals treated with wet oxygen at  $900^\circ\text{C}$  for 10 h.

at about  $3510\text{ cm}^{-1}$ . It has been concluded that the preferred plane of vibration of the hydroxyl ions is the plane perpendicular to  $c$ , while a small amount of  $\text{OH}^-$  ions vibrates along the  $c$  axis. This result has been confirmed for congruently melting SBN by us and we have proved that it holds for other  $x$  compositions, too. This is in contrast to PBN [35, 36] and KLN [37, 38] where a comparably strong absorption has been observed for extraordinarily polarized light, too. In the following sections we discuss only the  $\text{OH}^-$  spectra for ordinary light polarization.

A search for the influence of the ferroelectric phase transition on the  $\text{OH}^-$  stretch mode spectrum failed. The spectra of four samples with  $x$  values of (0.477, 0.511, 0.563, 0.644) in the range  $30 < T < 200$  revealed a linear red-shift of about  $13\text{ cm}^{-1}$  with increasing temperature ( $0.0765\text{ cm}^{-1}\text{K}^{-1}$ ). The observations reported recently [33] were confirmed for not congruently melting samples. No remarkable broadening was observed, but the maximum absorption decreased with increasing temperature and the spectrum became more symmetric.



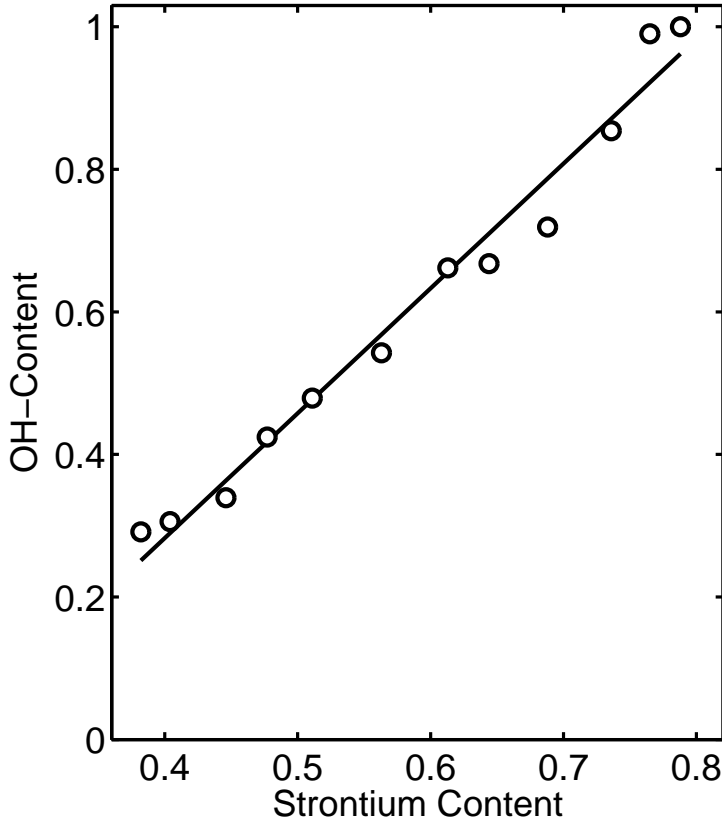


Figure 3.9: Normalized integral absorption of the OH<sup>-</sup> stretch mode for various Sr<sub>x</sub>Ba<sub>1-x</sub>Nb<sub>2</sub>O<sub>6</sub> crystals treated with wet oxygen at 900 °C for 10 h.

### Data Fiting

The shape of the OH<sup>-</sup> absorption bands is complex for each composition. It can be characterized by a main component peaking at about 3493 cm<sup>-1</sup> and a shoulder at the low energy side. While the main component is present in samples of all compositions, and only its intensity increases with  $x$ , as emphasized above, the shoulder changes more drastically. At low  $x$  (e.g.,  $x = 0.385$ ) the shoulder is present at about 3450 cm<sup>-1</sup>, while at high  $x = 0.788$  it appears as a sideband at about 3350 cm<sup>-1</sup>. The higher the  $x$ -values, the more symmetrical the main line.

The components of the complex absorption band in Sr<sub>x</sub>Ba<sub>1-x</sub>Nb<sub>2</sub>O<sub>6</sub> crystals are assumed to originate from vibrations of OH<sup>-</sup> ions in different environments. In order to find correlation between the structure of SBN and the possible hydrogen sites in the crystals the change of the band shape has to be characterized quantitatively for different compositions. In other words, the occupancy of the OH<sup>-</sup> defect sites can be deduced from the intensities of the band components. For this purpose the absorption bands have been decomposed into several components using a nonlinear least squares method.

First of all the decomposition procedure requires some knowledge about the number of components and the shape of each band. This is not obvious for strongly overlapping bands like in our case. A first hint can be obtained by an inspection of the high energy wing of the main line. This clearly points to a Gaussian, while the broad feature shifting from about  $3450\text{ cm}^{-1}$  to  $3350\text{ cm}^{-1}$  suggests a Lorentzian line shape. The asymmetry of the main band for low and medium  $x$ -values led us to include another band at about  $3455\text{ cm}^{-1}$ , but we have no conclusive arguments for a particular band shape, even if we take into account, that typically homogeneous broadening causes a Lorentzian shape, as it is observed for most of the  $\text{OH}^-$  stretching vibrational bands in other oxide crystals [31]. As a first attempt, called fit 1, we fitted each spectrum with three bands by varying the relevant parameters like position, linewidth and height. As expected from Fig. 3.8, the position and halfwidth of the main line are practically constant, but to our surprise the same holds for the second line at about  $3455\text{ cm}^{-1}$ , too. As it is seen in Fig. 3.10 the third

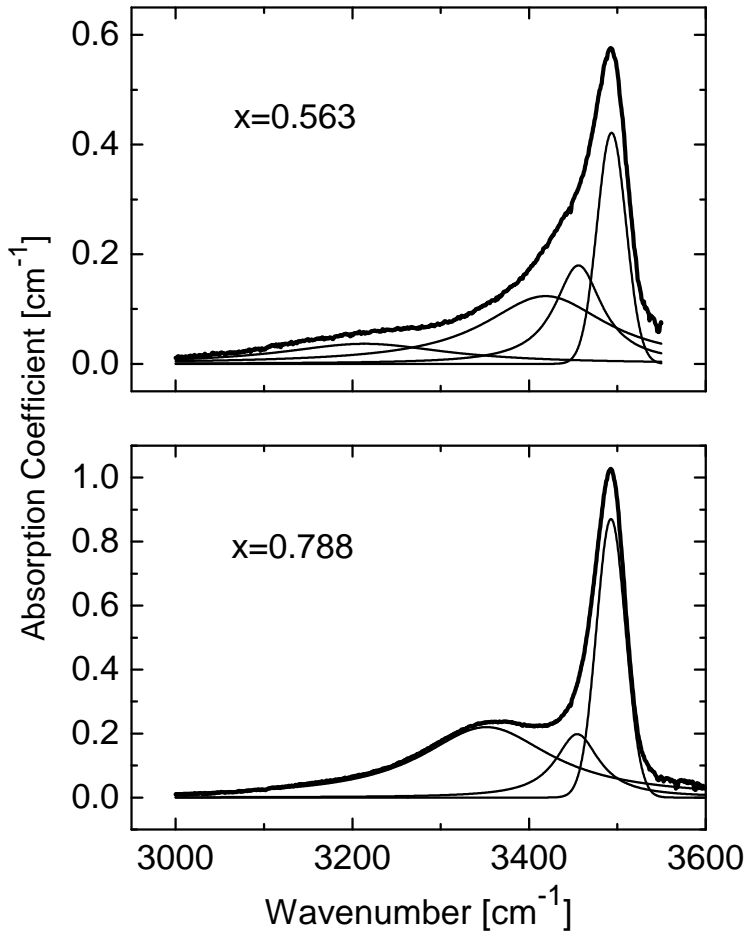


Figure 3.10: Decomposition of ordinarily polarized absorption spectra of the  $\text{OH}^-$  stretch mode in  $\text{Sr}_x\text{Ba}_{1-x}\text{Nb}_2\text{O}_6$  crystals with two different compositions. Different scales have been used for the ordinates.

line is shifted to lower energy with increasing  $x$ . For several compositions in the range

$x = 0.5 - 0.6$  the contribution of a weak and broad fourth component was also observed at about  $3220 \text{ cm}^{-1}$  (see the upper curve in Fig. 3.10). This band improved the quality of the fit, but did not influence strongly the parameters of the three other lines. Even more important was the observation, that all parameters varied without strong oscillations. This raised our hope to take up a satisfactory fit of all spectra at the same time with three bands as a function of the composition  $x$ . As a preparation for such a general fit, the data set, i. e. each spectrum, was smoothed using Savitzky-Golay filtering. Thus we get rid of noise and do not lose any spectral relevant information, because of the large halfwidth of the contributing bands.

Starting from the results of fit 1 and from the observation that the  $\text{OH}^-$  band intensity increases with  $x$ , the global description of the 12 spectra  $S$  was looked for using the form

$$S(x) = (a_1 + b_1x) \cdot G_1 + (a_2 + b_2x) \cdot L_1 + (a_3 + b_3x) \cdot L_2, \quad (3.13)$$

where  $G$  and  $L$  denote Gaussian and Lorentzian, respectively. For the position of the second Lorentzian –  $\tilde{\nu}_3$  –, as a conclusion of fit 1, a linear dependence on the composition  $x$  is assumed

$$\tilde{\nu}_3 = \tilde{\nu}_{30} - x \cdot d\tilde{\nu}_3, \quad (3.14)$$

where  $\tilde{\nu}_{30}$  is the extrapolated line position for SBN crystals with zero strontium content ( $x = 0$ ).

Fit	#1	#2	#3	#4
$l_1$ norm	0.0495	0.0926	0.0783	0.0757
No. of param.	108	13	14	17

Table 3.4: The  $l_1$  norm for the different fits.

This simulation of all spectra, called fit 2, depends on 13 parameters, as compared to the  $12 \times 9 = 108$  parameters of fit 1, see Table 3.4. The relatively good fit obtained by using only 13 parameters reflects that the assumption of fixed wavenumbers and halfwidths for the components was realistic. The right side of Fig. 3.11 shows, however, that some deviation between the measured and fitted data occurs mainly for the main component of the absorption spectrum. The deviations can be removed by introducing a quadratic term in the composition dependence of the main line

$$S'(x) = (a_1 + b_1x + c_1x^2) \cdot G_1 + (a_2 + b_2x) \cdot L_1 + (a_3 + b_3x) \cdot L_2. \quad (3.15)$$

Fig. 3.11 (left side) shows the result of fit 3 taking into account the nonlinear term for the Gaussian line. The parameter values of fit 2 and fit 3 are given in Table 3.5. The quality of the fit was quantitatively characterized by the well known  $l_1$  norm (the sum of the absolute differences between the theoretical curve and the experimental points). Lower values mean better quality here. Table 3.4 summarizes the quality factors obtained for the different fits. It is clearly seen that the quadratic dependence of the amplitude of the Gaussian line on composition improves the quality factor. A further, but very weak improvement could be achieved by assuming a fourth component of the absorption band at the low energy side (fit 4). This will be neglected further on.

Parameter	fit #2 ( $\text{cm}^{-1}$ )	fit #3 ( $\text{cm}^{-1}$ )
$\tilde{\nu}_1$	3492.5	3492.3
$\tilde{\nu}_2$	3455.6	3454.1
$\tilde{\nu}_{30}$	3546.3	3558.0
$d\tilde{\nu}_3$	244.3	259.4
$\sigma_1$	22.9	23.2
$\sigma_2$	28.8	30.0
$\sigma_3$	73.1	76.2
$a_1$	-0.430	0.574
$a_2$	0.046	0.099
$a_3$	-0.126	-0.161
$b_1$	1.608	-1.998
$b_2$	0.232	0.137
$b_3$	0.411	0.458
$c_1$	n. a.	3.072

Table 3.5: Values of all necessary fit parameters for the full global fits #2 and #3. The parameters  $\tilde{\nu}_i$  and  $\sigma_i$  represent the frequency and halfwidth of the components, respectively.

## Discussion

Let us summarize the main results of our extended curve fitting with the help of Fig. 3.12, where we used the parameters in Table 3.5 to plot the dependence of the wavenumber and amplitude of the bands on the strontium content. Two bands do not depend on  $x$  with respect to the line position, while the frequency of the third component decreases with increasing Sr content. The amplitude of the main band is always much stronger than that

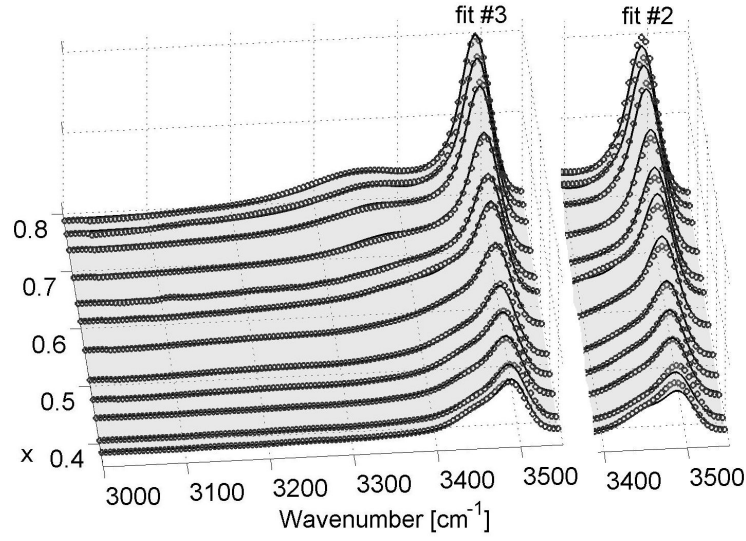


Figure 3.11: Three-line fits for the  $\text{OH}^-$ -Bands in SBN as a function of the composition. Solid black lines indicate fits, measured spectra are represented by the dots.

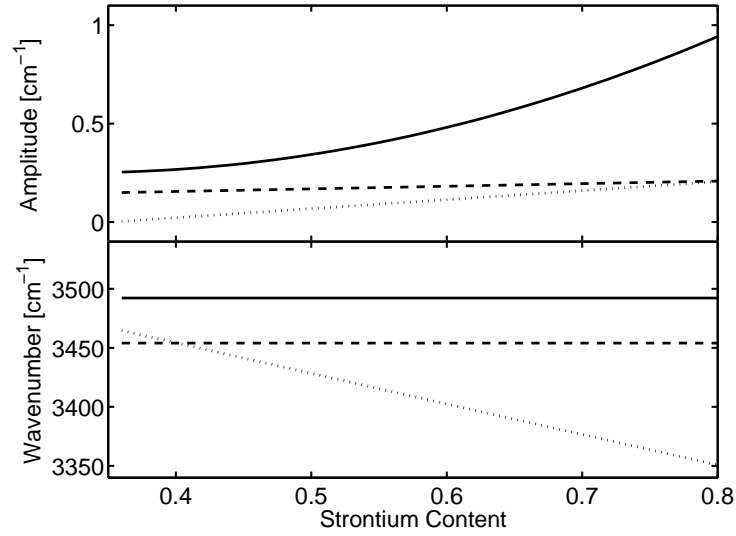


Figure 3.12: Composition dependence of the wavenumber and the corresponding amplitude for the three bands used in fit 3. Solids lines belong to the Gaussian band 1, dashed to component 2, while band 3 is represented by dotted lines.

of the other bands and depends in a slightly nonlinear manner on  $x$ . The amplitude of the second band is almost constant, while the contribution of the third band is remarkable at high Sr content. It is worth to mention, although not plotted, that the halfwidth of the bands was found to be unchanged in the whole composition range. The relatively broad bands are characteristic for the  $\text{OH}^-$  absorption lines in crystals belonging to the  $\text{LiNbO}_3$

family and other niobates having the tungsten bronze-type structure [31], and are related to the high number of structural defects due to the random distribution of strontium over the corresponding sites.

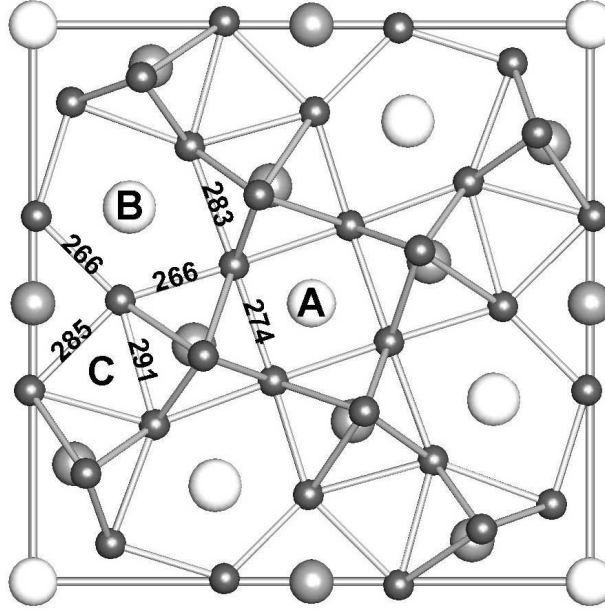


Figure 3.13: Schematic drawing and O–O bond lengths of the plane perpendicular to the tetragonal  $c$  axis of SBN. Tetragonal channel, partially occupied by Sr, A, pentagonal channel, partially occupied by Sr and Ba, B, and the empty triangular channel, C.

Thus we are searching for different lattice sites for the  $\text{OH}^-$  ions, which on one hand, are strongly influenced, and on the other hand, are nearly unaffected by the change of the Sr content. The SBN structure is built up of  $\text{NbO}_6$  octahedra which are linked via oxygen corners as mentioned in the introduction [18]. Because there are two independent  $\text{NbO}_6$  octahedra, the tetragonal network has three kinds of structural channels running along the  $c$ -axis A, B and C, see Fig. 3.13. The smallest one with a triangle shape is unoccupied in SBN, while the tetragonal and the pentagonal ones are partially filled. The medium-sized tetragonal channels contain Sr and the site occupancy is about 72% almost irrespective of  $x$ , the Sr content. The large pentagonal channel is a host for both Ba and Sr. The Ba ions occupy a site with mirror symmetry, while the Sr site in the pentagonal channel has no symmetry, because it is shifted by about  $\pm 25.5$  (29.2) pm for  $x = 0.75$  (0.61) out of the symmetry plane [18] depending on the composition. At low  $x$  values the pentagonal channel contains only Ba and no Sr.

With the information deduced from the composition dependence of the  $\text{OH}^-$  absorption spectra a more specific model for the hydrogen sites can be proposed. Sites for most of the hydrogen present in the crystal have to be restricted to the a,b plane, shown schematically in Fig. 3.13 because of the polarization behavior of the stretch mode absorption. The possible hydrogen sites are along the various O-O bonds in this plane. Such O-O bonds ranging from 265 to 291 pm form the equatorial planes of the two different  $\text{NbO}_6$  octahedra. As a general trend, the longer the O-O bond, the higher the frequency of the  $\text{OH}^-$  vibration along that bond [39]. Following this line, the main band at  $3493\text{ cm}^{-1}$  would correspond to  $\text{OH}^-$  vibrations in the unoccupied triangular channel having about 285-290 pm O-O bonds. The second band at  $3455\text{ cm}^{-1}$  which is practically independent of  $x$  may correspond to the tetragonal channel having 274 pm O-O bond lengths and nearly constant Sr occupancy [18], while the third band with the lowest vibrational frequency may belong to the pentagonal channel. Three O-O bonds in the pentagonal channel are only 266 pm long. We may further assume that the  $\text{OH}^-$  vibrations responsible for the third band belong to those pentagonal channels which are occupied by Sr ions. On one hand the Sr occupancy of this site is proportional to  $x$  in agreement with the increasing  $\text{OH}^-$  band amplitude, and on the other hand the increasing shift of Sr out of the mirror plane with decreasing  $x$  causes a strongly changing environment and in turn a strong frequency shift of the  $\text{OH}^-$  band.

## 3.3 Raman Spectroscopy

### 3.3.1 Experimental setup

Raman scattering experiments have been performed in right-angle geometry using a Spex 14018 double monochromator and a 514.5 nm exciting line of an argon ion laser with 1.2 W at room temperature.

The Raman setup is shown in Fig. 3.14. The light from the laser is focused on the sample by the lens  $L_1$ . To obtain different scattering configurations we used two polarizers ( $P_1$ ,  $P_2$ ). With  $P_1$  we set the direction of polarization of the incoming light and with  $P_2$  the direction of the polarization of the scattering light. The scattered light is focused by the lens  $L_2$  on slit  $F_1$ . We used a  $\lambda/2$ -plate to rotated the polarization direction of the scattering light into the optimized direction of the gratings  $G_1$  and  $G_2$ . In our measurements the slits  $F_1$  and  $F_3$  of the double monochromator are set to  $100\ \mu\text{m}$  and the slitwidth of  $F_2$  is  $200\ \mu\text{m}$ . The double monochromator is connect to the computer and controlled by a program. It is possible to set the wavenumber with a precision of  $0.02\ \text{cm}^{-1}$ . The intensity at a certain wavenumber is read by computer using an acquisition card (PMS 300) from the photomultiplier. For changing of wavenumbers, reading of the intensity and recording this two values in files we made a program using Visual C++. The processing of these data was made with the help of a Matlab program.

In our measurement we used the SBN crystals with  $x = 0.38$  to  $0.78$ . The crystals were cut carefully, along a, b, and c axes, into samples with size of about  $4 \times 4 \times 6\ \text{mm}^3$ , then they were polished to optical quality.

### 3.3.2 Group Theoretical Considerations for Lattice Vibrations

The SBN crystal, crystallized in an unfilled TB type structure in the tetragonal crystal system belongs at room temperature to the space group  $P4bm$  and has five formula units per unit cell [14]. Therefore there are 135 vibrational modes ( $3 \times 45$ ) including three acoustic modes.

The reducible representations for the space group  $P4bm$  at the zone center  $\Gamma$  of the first Brillouin zone are given in Table 3.6, using The International Table for Crystallography [40].

Based on the factor group theory, the reducible representations shown in Table 3.6 can be



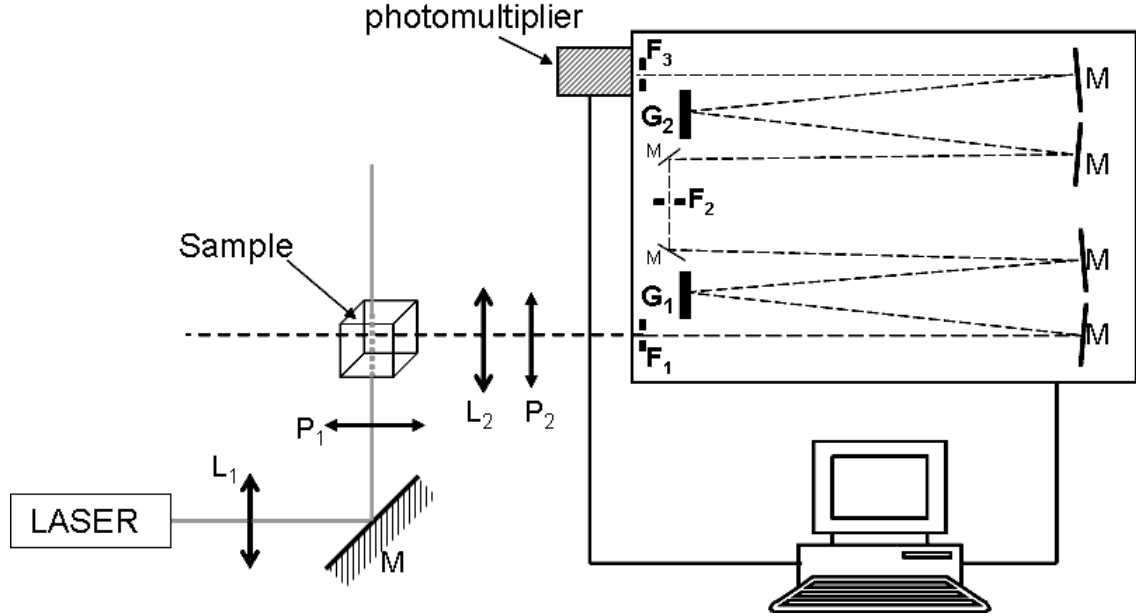


Figure 3.14: Sketch of the Raman setup.

symmetry operations	E	$2C_4(z)$	$C_2$	$2\sigma_v$	$2\sigma_d$
Wyckoff position	8d	24	0	0	0
and character	4c	12	0	0	2
	2b	6	0	-2	0
	2a	6	2	-2	0

Table 3.6: The reducible representations for  $P4bm$  at the  $\Gamma$  point [41]

reduced as follows [42]:

$$\begin{aligned}
2a: & 1A_1 + 1A_2 + 2E; \\
2b: & 1A_1 + 1B_2 + 2E; \\
4c: & 2A_1 + 1A_2 + 1B_1 + 2B_2 + 3E; \\
8d: & 3A_1 + 3A_2 + 3B_1 + 3B_2 + 6E.
\end{aligned}$$

The matrices for the components of the Raman tensor for irreducible representations of the  $4mm$  group are [43]

$$\begin{aligned}
 A_1(z) &= \begin{pmatrix} a & 0 & 0 \\ 0 & a & 0 \\ 0 & 0 & b \end{pmatrix} & B_1 &= \begin{pmatrix} c & 0 & 0 \\ 0 & -c & 0 \\ 0 & 0 & 0 \end{pmatrix} & B_2 &= \begin{pmatrix} 0 & d & 0 \\ d & 0 & 0 \\ 0 & 0 & 0 \end{pmatrix} \\
 E(x) &= \begin{pmatrix} 0 & 0 & e \\ 0 & 0 & 0 \\ e & 0 & 0 \end{pmatrix} & E(y) &= \begin{pmatrix} 0 & 0 & 0 \\ 0 & 0 & e \\ 0 & e & 0 \end{pmatrix}
 \end{aligned}$$

The symmetry species  $A_1(z)$ ,  $E(x)$ , and  $E(y)$  show dipole moments oriented along the Z-, X-, and Y-directions, respectively. Because of equivalence of the axes X and Y for the measurement of Raman spectra of uniaxial crystals with point group  $4mm$  [14], the interesting geometrical configurations are X(ZZ)Y, X(YZ)Y, X(YX)Y, and X(YY)Z. All the bands in the X(ZZ)Y spectrum originate from transverse phonon modes with polarization along the Z axis. They are denoted  $TA_1$ . The bands in the X(YZ)Y spectrum arise from both longitudinal and transverse modes polarized perpendicular to the Z axis. They are designed LE and TE. The X(YX)Y bands are all of species  $B_2$ . Finally, the X(YY)Z bands belong to the the symmetry species  $A_1$  and  $B_1$ . The  $A_1$  modes are quasi-longitudinal (QL) and quasi-transverse (QT), where the  $B_1$  modes have no polarization [44, 45].

We have seen that the spectrum of the lattice vibrations of the octahedral ion  $[NbO_6]^{7-}$  in some crystals, such as the filled TB type barium sodium niobate (BNN) [46, 41], potassium lithium niobat (KLN) [42] and non-TB type  $LiNbO_3$  crystals [47, 48], are similar to each other and share some common characteristics.

An octahedral molecule  $XY_6$  with the symmetry  $O_h$  has 15 internal vibrational degrees of freedom or six normal vibrational modes  $\nu_i$ , as it is shown in Fig. 3.15. They can be represented from group theoretical considerations as

$$\Gamma'_{vib} = A_{1g}(R) + E_g(R) + 2T_{1u}(IR) + T_{2g}(R) + T_{2u}(inactive), \quad (3.16)$$

where the subscripts  $g$  and  $u$  represent symmetric and antisymmetric vibrations, respectively. The modes  $\nu_1(A_{1g})$ ,  $\nu_2(E_g)$ , and  $\nu_3(T_{1u})$  are all stretch vibrations and  $\nu_4(T_{1u})$ ,

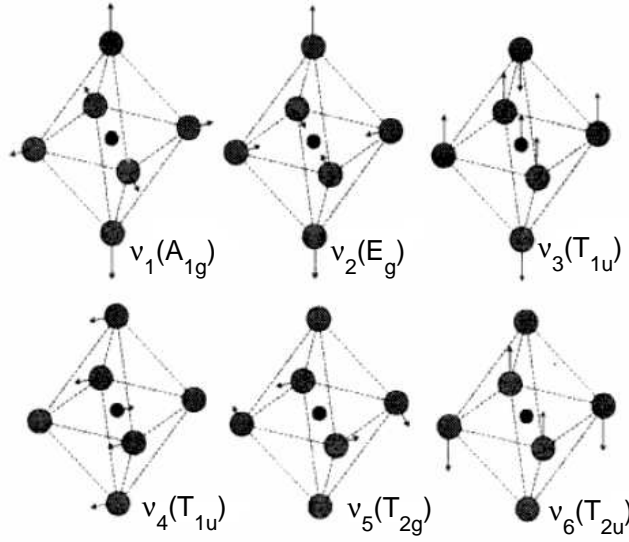


Figure 3.15: The normal vibration modes of an octahedron molecule  $XY_6$  with the symmetry  $O_h$ .

$\nu_5(T_{2g})$ , and  $\nu_6(T_{2u})$  are all bend vibrations [42]. Thus there might be three characteristic Raman peaks in the SBN, which belong to the internal vibration modes of the octahedral ion  $[\text{NbO}_6]^{7-}$ . In a primitive cell of the SBN, there are ten Nb-O octahedral ions.

### 3.3.3 Results and Discussion

Fig. 3.16 shows the typical Raman spectra of the crystals with Nb-O octahedron ions, recorded in SBN for different values of the composition at room temperature in the frequency range from 20 to  $1000\text{ cm}^{-1}$ , with the scattering geometry  $X(\text{ZZ})Y$ , corresponding to the symmetry species  $A_1$ , concerning extraordinary transverse optical phonons propagating along the  $[1\bar{1}0]$  direction. The spectra were shifted vertically for a better viewing. Compared with other Raman spectra of the TB crystal [46, 41, 42] it is easy to determine the three characteristic Raman peaks of  $[\text{NbO}_6]^{7-}$  in the SBN to be at about 850, 630 and  $260\text{ cm}^{-1}$ . All these three peaks have a shoulder at the low energy side. This behavior is probably due to the fact that in a SBN crystal two types of the  $[\text{NbO}_6]^{7-}$  octahedra exist. The low frequency bands probably arise from motions of the Ba and Sr ions and also from the external vibrational modes of the octahedral ion  $[\text{NbO}_6]^{7-}$ .

Fig. 3.17 shows room temperature Raman spectra of SBN in the  $X(\text{YZ})Y$  scattering con-

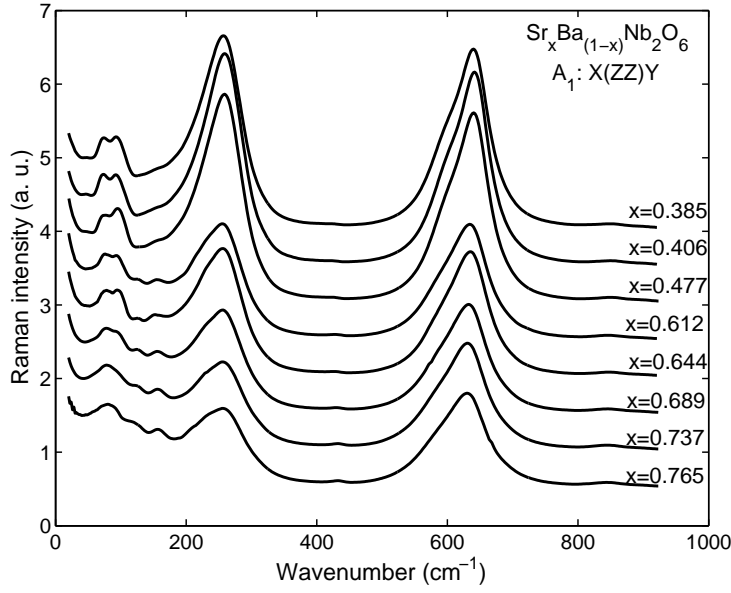


Figure 3.16: The Raman spectra for various  $\text{Sr}_x\text{Ba}_{1-x}\text{Nb}_2\text{O}_6$  crystals with the scattering geometry  $X(ZZ)Y$ .

figuration, which correspond to the symmetry species E and involving ordinary transverse and extraordinary longitudinal optical phonons propagating along the  $[1\bar{1}0]$ .

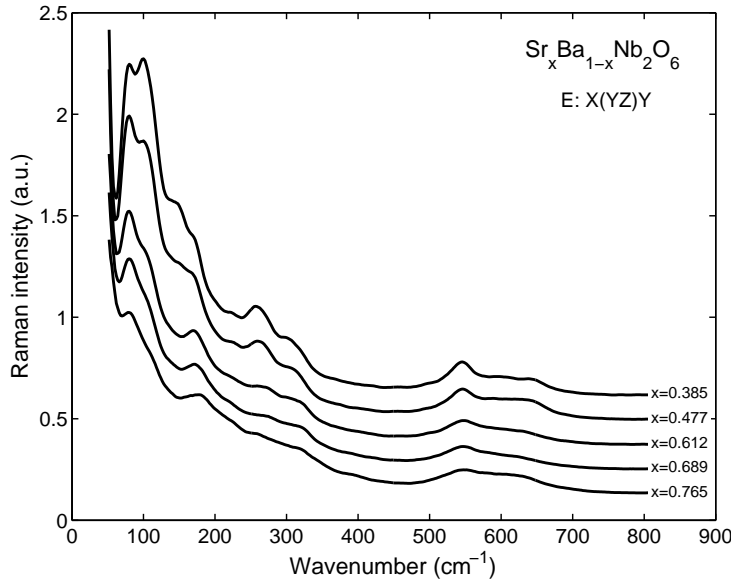


Figure 3.17: The Raman spectra for various  $\text{Sr}_x\text{Ba}_{1-x}\text{Nb}_2\text{O}_6$  crystals with the scattering geometry  $X(YZ)Y$ .

Fig. 3.18 shows a room temperature Raman spectrum of SBN for a  $X(YX)Y$  scattering configuration, belonging to the symmetry species  $B_2$ .

Fig. 3.19 shows a room temperature Raman spectrum of the SBN with a scattering geom-

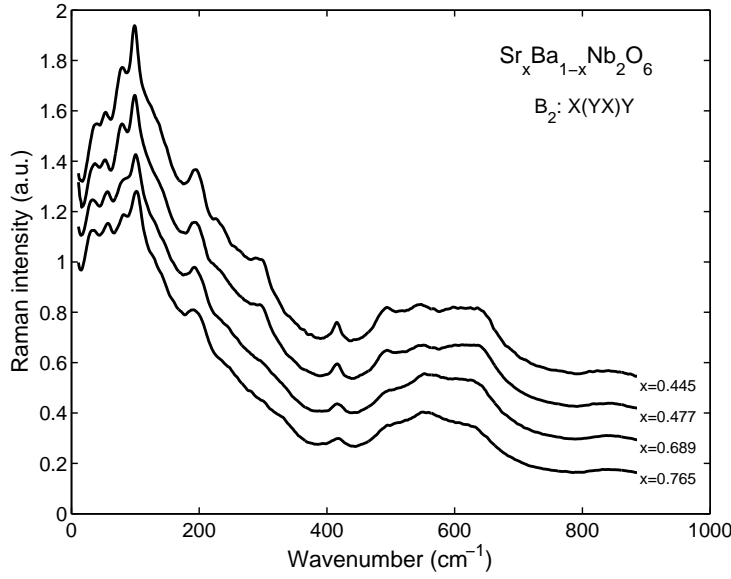


Figure 3.18: The Raman spectra for various  $\text{Sr}_x\text{Ba}_{1-x}\text{Nb}_2\text{O}_6$  crystals with the scattering geometry  $\text{X}(\text{YX})\text{Y}$ .

etry  $\text{X}(\text{YY})\text{Z}$  corresponding to the species  $\text{A}_1$  and  $\text{B}_1$ .

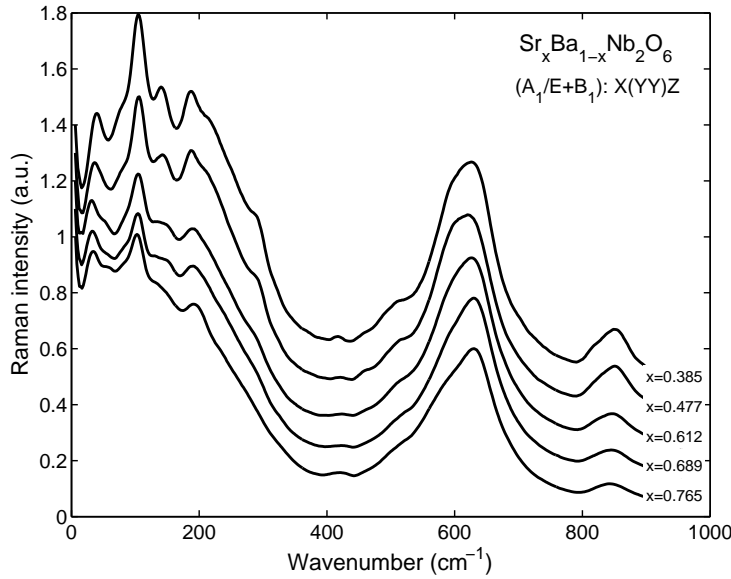


Figure 3.19: The Raman spectra for various  $\text{Sr}_x\text{Ba}_{1-x}\text{Nb}_2\text{O}_6$  crystals with the scattering geometry  $\text{X}(\text{YY})\text{Z}$ .

The frequency assignments of the lattice modes of the SBN crystal and the relative parameters are reported in Table 3.7, where  $\alpha_{ZZ}$ , etc. represent the polarizability tensor elements.

Comparing the lattice-vibration spectra of SBN with different compositions we can see the influence of the Sr/Ba ratio on the characteristic Raman spectra of the  $[\text{NbO}_6]$  octahedra. For the tetragonal TB type crystals the Raman spectra are similar to each other, and the

Symmetry species	X(ZZ)Y TA <sub>1</sub>		X(YZ)Y LE, TE		X(YX)Y B <sub>2</sub>		X(YY)Z QL, QT, B <sub>1</sub>	
x	0.406	0.737	0.406	0.737	0.406	0.737	0.406	0.737
Raman results	$\alpha_{ZZ}$		$\alpha_{YZ}$		$\alpha_{YX}$		$\alpha_{YY}$	
	74	79	80	80	39	33	39	33
	93	-	100	105	54	57	105	104
	-	125	150	-	79	80	142	140
	156	156	170	173	99	101	187	190
	259*	257*	259*	257*	125	-	290	-
	642*	631*	299	315	196	190	515	-
	850*	844*	546	548	293/297	-	626*	632*
			602/642*	589/631*	416	416	851*	844*
					492	492		
					546	546		
					602/642*	589/631*		

Table 3.7: The assignments of the lattice-vibration for the SBN. \* - characteristic Raman peaks of  $[\text{NbO}_6]$  octahedra

common characteristics are the following: (1) the octahedral ion  $[\text{NbO}_6]^{7-}$  in the crystals has three characteristic Raman peaks, two of them having relatively large Raman intensity; (2) all Raman lines are very broad; (3) at low wavenumbers the scattering-background is very strong; (4) the detected Raman lines are much fewer in number than those calculated by group theory.

In the next part we have focused on the mode at around  $630 \text{ cm}^{-1}$  in the X(ZZ)Y scattering configuration because it has relative large Raman intensity and very small background. We fitted this mode for each composition with two bands by varying the parameters like position, halfwidth and amplitude. Fig. 3.20 shows a decomposition of the mode at about  $630 \text{ cm}^{-1}$  for two different compositions. We associate the intense band to the  $[\text{NbO}_6]_{II}$  octahedra because in the structure of the SBN exists eight  $[\text{NbO}_6]_{II}$  octahedra and two  $[\text{NbO}_6]_I$  octahedra per unit cell. At first look it is possible to observe a shift to lower energy of both bands with increasing  $x$ . Also the intensity of the bands decreases with increasing the composition  $x$ .

The fit results are presented in Fig. 3.21 where is plotted the dependence of the amplitude, halfwidth and position of the bands depending as function of the strontium content. Between the length of the Nb-O bond and the vibration frequency of Nb-O exists a corre-

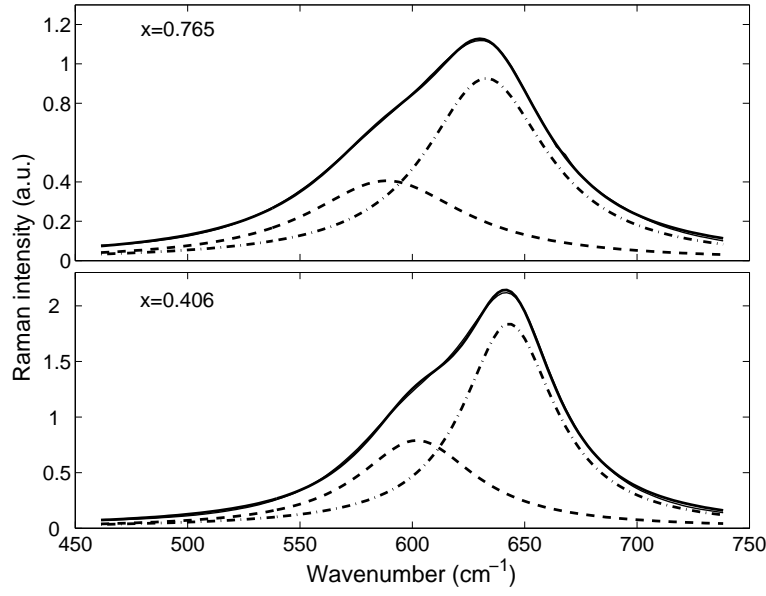


Figure 3.20: Decomposition of the mode at about 630 cm<sup>-1</sup> recorded in the X(ZZ)Y scattering geometry for two different compositions.

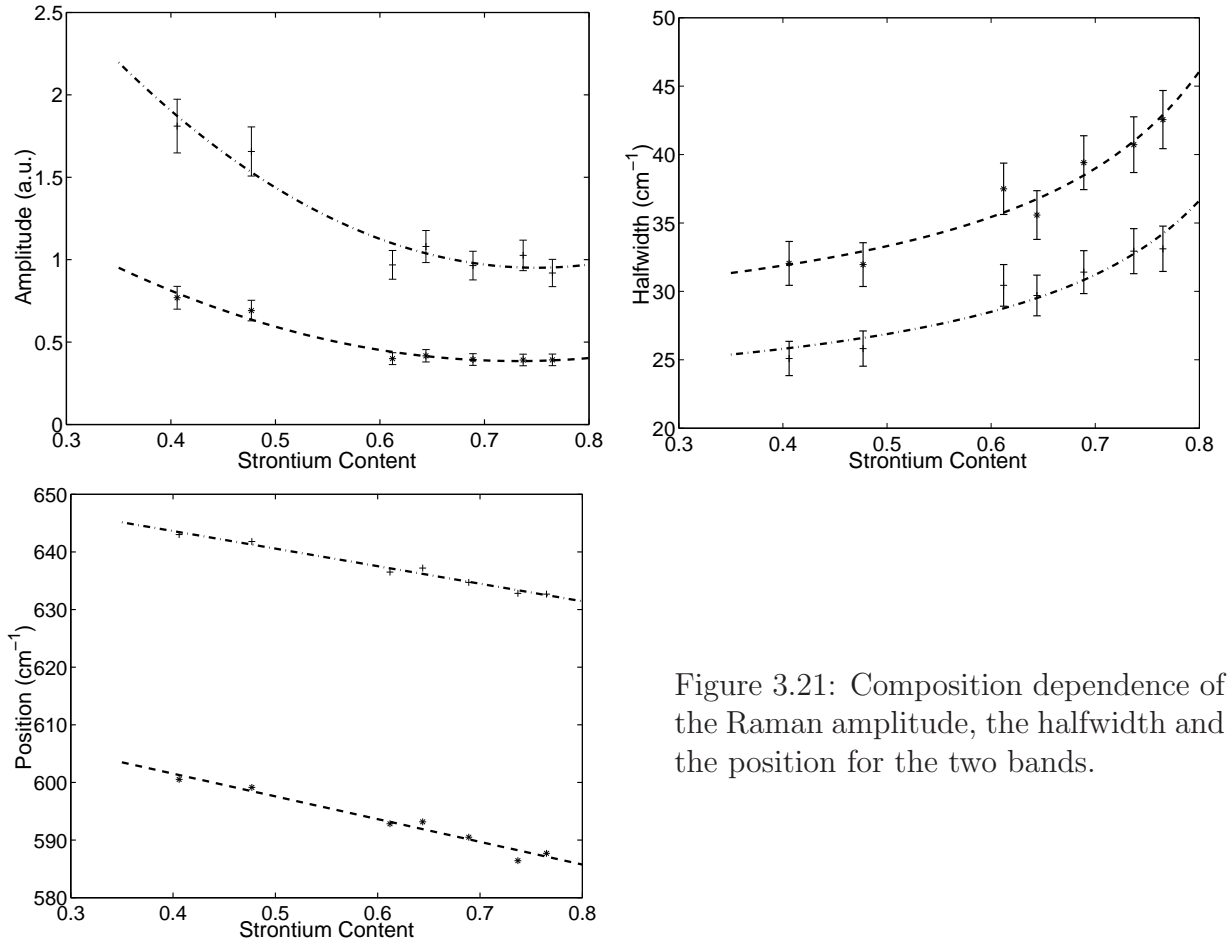


Figure 3.21: Composition dependence of the Raman amplitude, the halfwidth and the position for the two bands.

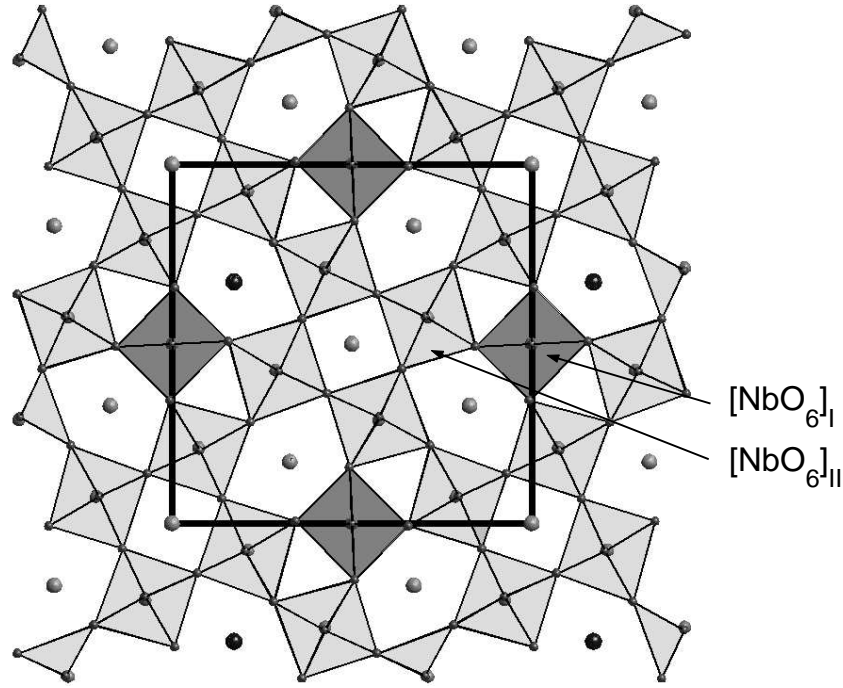


Figure 3.22: Projection of the SBN structure onto the  $ab$  coordinate plane.

lation, so, any modification that appear in the length of the Nb-O bond will be reflected in the vibration frequency of Nb-O.

If we consider the position dependence of the two bands as a function of concentration (Fig. 3.21) we can observe a linear shift to lower energy. This shift can be correlated with a linear variation of the Nb-O bonds length (average). This idea is confirmed in the articles [16, 18] where are calculated the interatomic distances in the SBN with different compositions. The length of Nb-O bonds decrease with increasing the Sr content.

The halfwidth determined from our measurements can be associated with distortions of the  $\text{NbO}_6$  octahedra ( $\Delta[\text{Nb-O}]$ ). In Fig. 3.21 the values of the halfwidth corresponding to the  $[\text{NbO}_6]_{\text{I}}$  octahedra are higher than the values for the  $[\text{NbO}_6]_{\text{II}}$  octahedra. That means  $\Delta[\text{Nb-O}]_{\text{I}}$  is larger than  $\Delta[\text{Nb-O}]_{\text{II}}$ , this is confirmed in the reports [16, 18]. Also in this figure it is possible to observe an increase of the halfwidth with increasing Sr content. The explanation of this is given by the channels that surround all type of  $\text{NbO}_6$  octahedra.  $[\text{NbO}_6]_{\text{II}}$  octahedra are surround by two pentagonal channels, one tetragonal and one triangular channel and  $[\text{NbO}_6]_{\text{I}}$  octahedra are surrounded by two pentagonal channels and two triangular channels (Fig. 3.22). Because the triangular channels are empty and tetragonal channels are occupied only by Sr atoms, the variation of  $\text{NbO}_6$  octahedra is not



influence by these channels. The distortion of the  $\text{NbO}_6$  octahedra is mainly due to the Ba and Sr atoms in the pentagonal channels. Considering a SBN structure in which five-fold channels are occupied only by Ba atoms, the  $\text{NbO}_6$  octahedra contained in this structure are almost identical ( $\Delta[\text{Nb-O}]$  is smaller). By increasing the Sr content in the SBN crystal, there will be more Sr atoms occupying the five-fold channels. As a consequence the  $\text{NbO}_6$  octahedra will be distorted due to different type of atoms around them. This means that if we consider two  $\text{NbO}_6$  octahedra, but the same types ( $[\text{NbO}_6]_I$  or  $[\text{NbO}_6]_{II}$ ), in different surrounding, the deformation will not be the same (the length of Nb-O bonds varies over a broad range of values,  $\Delta[\text{Nb-O}]$  is larger)

We can conclude that the variation of the length of the Nb-O bonds from both  $\text{NbO}_6$  octahedra is directly proportional to the Sr/Ba ratio in the pentagonal channels. In this case we fitted the halfwidth of the bands corresponding to different  $\text{NbO}_6$  octahedra with the following equation:

$$\text{Halfwidth}(x) = a \frac{x - x_1}{1 - x} + b \quad (3.17)$$

where  $(x - x_1)/(1 - x)$  represents the Sr/Ba concentration ratio in pentagonal channels,  $x_1$  represents the concentration of Sr in the tetragonal channel, a and b are constants.

Using this results, a qualitative analysis of the  $\text{NbO}_6$  octahedra deformation as a function of the composition is obtained.

# Chapter 4

## Dielectric Properties

### 4.1 Composition dependence of the phase transition temperature. Pyroelectric Measurement

#### 4.1.1 Experimental setup

The experimental setup is presented in figure 4.1. This setup was constructed to permit four usage modes:

1. hysteresis measurement
2. conductivity measurement
3. pyroelectric measurement
4. polarization

The components used for building the setup are:

- an electrometer charge measuring device (Keithley 6514)
- a high voltage amplifier (610C from Trek)
- a temperature controller (PRO800 from Profile for the Peltier element and CAL3300 from CAL Controls for the resistance)

All this three components are connected to a computer using an IEEE 488 interface card and a RS-232 interface. For controlling, reading and recording of the data from this devices, we wrote a programme using Visual C++.

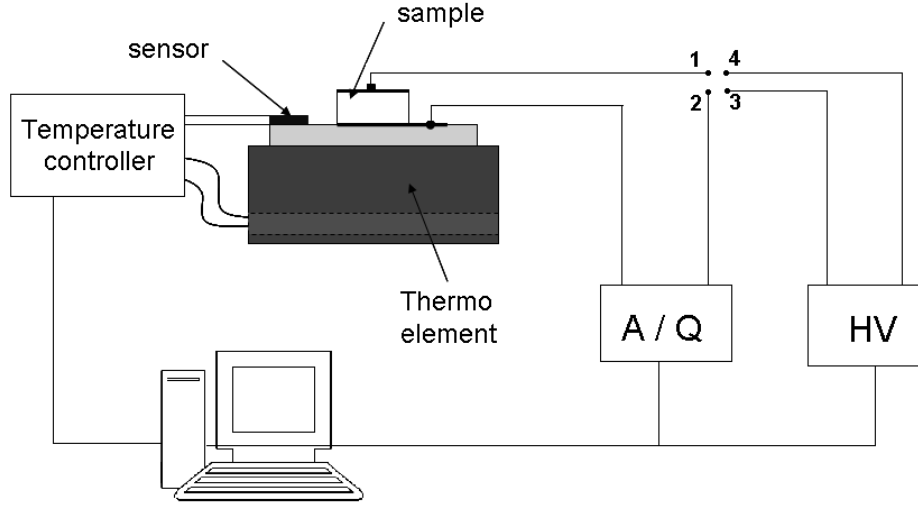


Figure 4.1: Sketch of the pyroelectric setup.

For a measurement the samples are placed on the thermo-controlled plate which can fix the temperature with an accuracy of  $0.1^\circ\text{C}$  in a range from  $-10^\circ\text{C}$  up to  $200^\circ\text{C}$  when using the Peltier element and  $30^\circ\text{C}$  up to  $260^\circ\text{C}$  with the resistance. The charge accumulation is measured with an accuracy of  $0.01\text{ nC}$ , typically corresponding to an error of  $0.0001\%$  in our measurement.

#### 4.1.2 Results and discussion

As shown in figure 4.1 there are four connectors and we make different connections between them depending on the type of measurement. For a pyroelectric measurement we connect 1–2. In these measurements we used  $\text{Sr}_x\text{Ba}_{1-x}\text{Nb}_2\text{O}_6$  crystals from melts with a Sr fraction in the range of 0.19 to 0.84, which corresponds to 0.32 to 0.82 in the samples. The crystals were cut into platelets with a thickness of 2 mm along the crystallographic axis.

To obtain a fully poled sample, we used the same setup with the following connections: 2–3 and 1–4. The crystal was heated up to a temperature exceeding the expected  $T_c$  (about  $50^\circ\text{C}$ ), estimated from a linear interpolation of known data [3, 49]. Then an electric field of  $350\text{ V/mm}$  was applied parallel to the  $c$ -axis, and the samples were cooled back to room temperature in 90 min with the field applied. This poling procedure was available for SBN crystals with  $x > 0.5$ . When  $x < 0.5$  it is not possible to apply  $350\text{ V/mm}$  because the electric conductivity of these crystals is higher and a current exceeding  $100\mu\text{A}$  will produce a damage. In this case we had increased the electric field until the current through the

sample was approximately  $70\mu A$ . Due to the current limitation, in some cases ( $x < 0.5$ ) only a small electric field could be applied. In this case we are interested to know if we obtain a fully poled samples. Trying to find the answer to this problem we made the following experiment.

For this experiment we used SBN crystal with  $x = 0.563$ . For the polarization, the crystal was heated to  $T = 150^\circ C$  (approximately  $50^\circ C$  more that the phase transition temperature), then an electric field of  $50 V/mm$  was applied parallel to the  $c$  axis and finally the temperature was slowly cooled down to room temperature. After polarization we made several pyroelectric measurements. These steps were repeated for each of the following values of the electric field:  $100 V/mm$ ,  $250 V/mm$  and  $400 V/mm$ .

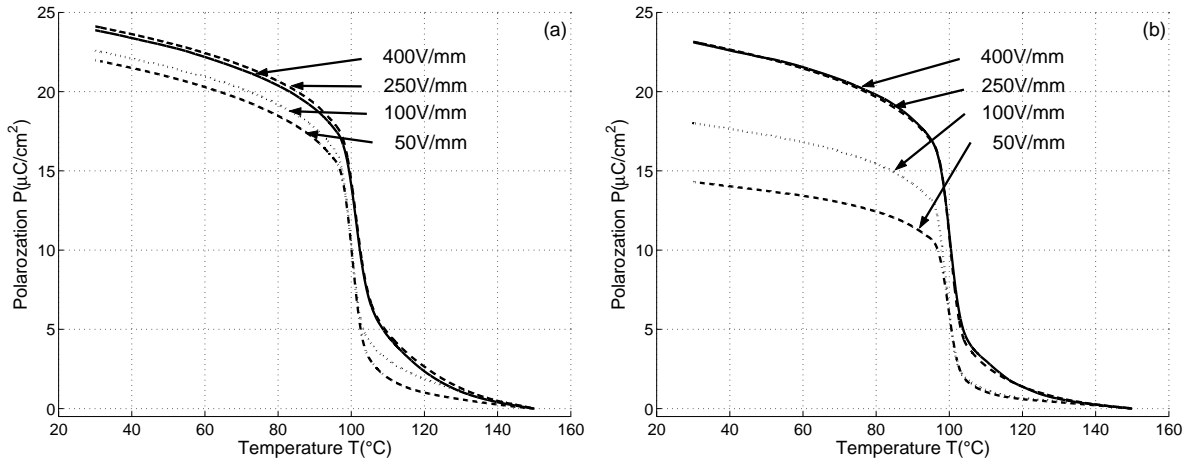


Figure 4.2:  $P(T)$  curves of  $Sr_xBa_{1-x}Nb_2O_6$  with  $x=0.563$  after to poled with difference values of the voltage 50, 100, 250 and 400 V/mm. (a) first pyroelectric measurement; (b) second pyroelectric measurement.

The transition from the paraelectric phase to the ferroelectric phase is accompanied by a small atomic displacements producing electric-dipole moments (domains) in the crystal. The symmetry of the ferroelectric phase is lower than the symmetry of the paraelectric phase. In our case SBN is a typical representative of tetragonal unfilled tungsten-bronze-type compounds. Within the tetragonal system it undergoes a relaxor phase transition from ferroelectric phase (point group  $4mm$ ) into the paraelectric phase ( $4/mmm$ ) [14, 50]. In the ferroelectric phase, the crystal contains needlelike  $180^\circ$  domains parallel to the crystallographic  $c$  axis, allowing only two equivalent polarization directions [51].

In case of applying a small electric field it is sufficient to force all domains turning in the same direction when cooling below the phase transition. As it is show in fig. 4.2(a) in all

cases the spontaneous polarization has the same value. With a high electric field applied some defects appear which induces a preferred direction of the ferroelectric domains in the crystal which is stable in the paraelectric phase. This leads to a strong repoling of the crystal when cooling below the phase transition even in the absence of an external electrical field. We can observe in the fig. 4.2(b), where is shown the second pyroelectric measurement of the crystal, for an electric field higher than 250 V/mm, that a total repoling is obtained (memory effect).

Thus, we can obtain a fully poled sample in case we applied a small electric field when the sample is heated to a high temperature ( $T > T_c$ ) but in this case the sample, after one pyroelectric measurement, does not show a total repoling.

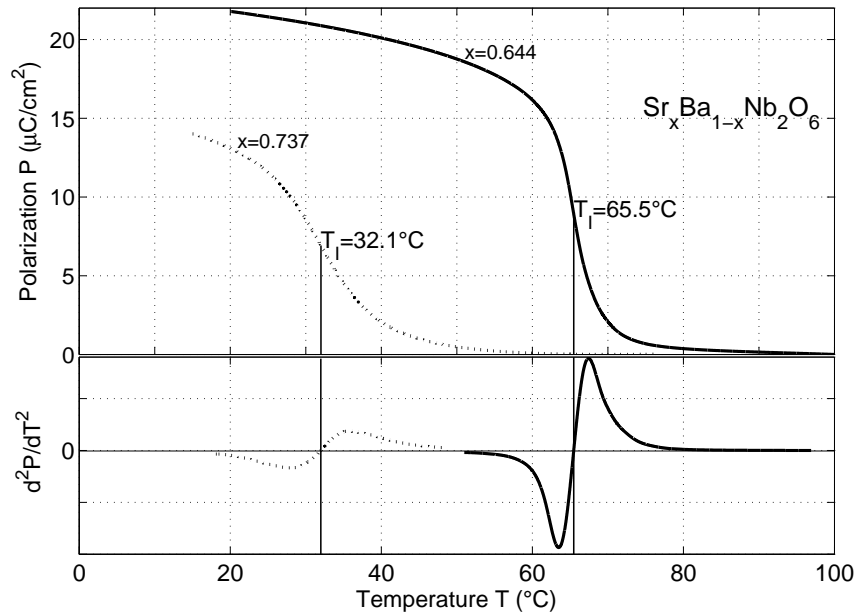


Figure 4.3:  $P(T)$  curves of  $\text{Sr}_{0.644}\text{Ba}_{0.356}\text{Nb}_2\text{O}_6$  and  $\text{Sr}_{0.737}\text{Ba}_{0.263}\text{Nb}_2\text{O}_6$ . The temperature  $T_I$  of the inflexion point was determined from the null of the second derivative  $d^2P/dT^2$ , shown in the lower part of the figure.

Figure 4.3 exemplarily shows  $P(T)$  for two samples with  $x = 0.644$  and  $x = 0.737$ . The temperature  $T_I$  of the inflexion point is marked by the zero crossing of the second derivative  $d^2P/dT^2$  which is shown in the lower part of Figure 4.3. The relaxor behavior is well emphasized in  $P(T)$  and the second derivative. It is most pronounced for larger  $x$  and decreases with decreasing  $\text{Sr}^{2+}$  concentration. Even a small variation of the Sr-content of less than 0.1 results in a remarkable change of the shape of  $P(T)$ , see Figure 4.3. For very high temperatures, the determination of  $P(T)$  became less reliable due to the high electric

conductivity of all samples: It was not possible to compensate external electric fields below the mV scale. In the paraelectric phase the electric conductivity of the samples became so large that these small fields were sufficient to cause electric currents which made effective surface charge measurements of the polarization impossible. However, direct measurements of the conductivity showed that this problem arose only at  $T > T_I + 15^\circ\text{C}$ .

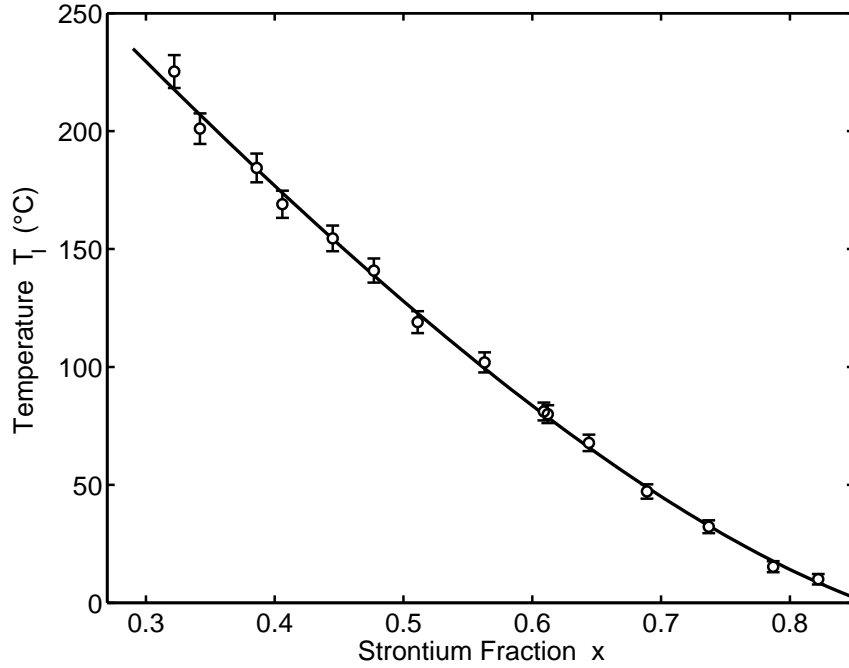


Figure 4.4: Temperature  $T_I$  for SBN as a function of the Sr-fraction  $x$ .

Figure 4.4 shows the dependence of  $T_I$  on the Sr fraction  $x$ . The continuous line, describing the measured data very well, represents a fit within the framework of an effective field approach, which will be discussed below.

The decrease of  $T_c$  with increasing Strontium content qualitatively agrees with observations reported in the literature [3, 49]. However, the transition temperatures shown here deviate from the literature values: we observed higher  $T_c$  for small values of  $x$  and lower  $T_c$  for high values of  $x$ . A possible explanation lies in the uncertainty of the composition of the samples used for earlier studies, where generally only the Sr-content in the melt is given. We have found that the actual Sr-content  $x$  in the sample tends to shift closer to the congruently melting composition,  $x = 0.61$ . This explains the systematic deviation of our  $T_c$  from earlier literature values. Furthermore, the transition temperatures reported earlier stem from dielectric measurements and are less reliable due to their frequency-dependence

[52, 53].

The nonlinear behavior of  $T_c(x)$  can be explained by structure induced polarization changes. SBN belongs to the structure type of the tetragonal tungsten bronzes, i.e., the structure consists of corner-linked  $NbO_6$  octahedra forming pentagonal, tetragonal and trigonal channels [14, 54]. Large  $Ba^{2+}$  ions occupy only the pentagonal channels, of which there are 4 per unit cell, while smaller  $Sr^{2+}$  ions occupy both the pentagonal and the tetragonal channels, of which there are 2 per unit cell. Approximately 72% of the tetragonal channel are occupied independent of the composition  $x$  with  $Sr^{2+}$ . However, the pentagonal channels are occupied by roughly 85% only by  $Ba^{2+}$  for  $x = 0.33$ , which decreases to circa 31% for  $x = 0.75$ , while the  $Sr^{2+}$  content increases from zero to about 57%, respectively. Because of the only Sr containing tetragonal channel and the strong variation of the Sr/Ba ratio in the pentagonal channel it is tempting to regard the compositional changes of  $Sr_xBa_{1-x}Nb_2O_6$  as being caused by three sub-lattices. Sub-lattice (1) may be devoted to Sr in tetragonal sites, (2) to Sr in pentagonal ones, while (3) is devoted to Ba. Within an effective field approach [55] the polarization of  $m$  coupled systems is described by  $m$  equations of the form:

$$P_i = N_i \mu_i \tanh \left( \frac{\left( E + x_i \beta_i P_i + \sum_{k \neq i} (x_k \alpha_{ik} P_k) \right) \mu_i}{k_B T} \right) \quad (4.1)$$

The parameters  $\alpha_{ik}$  describe the coupling strength between the subsystems with polarization  $P_i$ , the number of elementary dipoles  $N_i$ , the dipole moments  $\mu_i$  and the effective fields  $\beta_i$ , while  $k_B T$  has the usual meaning. The relative portions are  $x_i$  and  $\sum_i x_i = 1$ . For temperatures approaching  $T_c$  the polarization approaches zero, the hyperbolic tangent can be approximated by its argument. Summarizing several parameters in  $T_i = \beta_i N_i \mu_i^2 / k_B$ , which might be regarded as the Curie temperatures of the 'pure' sublattices, Eq. 4.1 transform to:

$$(a_{ki} - \delta_{k,i} T) P_i = b_i E_i \quad \text{with} \quad a_{ki} = \begin{cases} x_i T_i & \text{for } k = i \\ x_i T_i \alpha_{ki} / \beta_k & \text{for } k \neq i \end{cases}, \quad b_i = T_i / \beta_i \quad (4.2)$$

The polarizations should be able to approach any value at  $T_c$  at zero field. Therefore the

determinant of the coefficients must vanish. For  $m = 3$  we derive  $T_C^3 - s_2 T_C^2 + s_1 T_C - s_0 = 0$  with

$$s_2 = \sum_i a_{ii}, \quad s_1 = \sum_{i,k>i} (a_{ii}a_{kk} - a_{ik}a_{ki}), \quad s_0 = \sum_{i \neq k \neq l \neq i} (a_{i1}a_{k2}a_{l3}(-1)^{np(ikl)}) \quad (4.3)$$

and  $np(ikl)$  is the number of permutations necessary to produce the index set  $\{i, k, l\}$  from  $\{1, 2, 3\}$ . Because an exact solution is awkward to manage, we linearize the third order equation by substituting  $s_2 + \Delta$  for  $T_C$  and omitting all nonlinear terms in  $\Delta$ . Physically this is well justified as  $s_2$  is the 'classical' Curie temperature, the weighted sum over the Curie temperatures of the 'pure' sublattices  $s_2 = \sum_i a_{ii} = \sum_i (x_i T_i) = T_C^{classical}$  and only minor deviations are expected. We obtain:

$$T_C = s_2 + \frac{s_0 - s_1 s_2}{s_1 + s_2^2} \quad \text{with} \quad s_1 s_2 \gg s_0 \quad \text{and} \quad s_2^2 \gg s_1 \quad \text{and thus} \quad T_C = s_2 - \frac{s_1}{s_2} \quad (4.4)$$

The parameter  $s_1$  is a slightly more complex sum, but replacing the quotients  $(\alpha_{ik}\alpha_{ki})/(\beta_i\beta_k)$  therein by an appropriate average factor  $\lambda^2$  we arrive for the Curie temperature finally at:

$$T_C(x_i) = T_C^{classical} - \frac{1 - \lambda^2}{T_C^{classical}} \sum_{i,k>i} (x_i x_k T_i T_k) \quad (4.5)$$

We point out that for a system with two sublattices, the parameter  $(\alpha_{ik}\alpha_{ki})/(\beta_i\beta_k)$  reduces to  $(\alpha_{12}\alpha_{21})/(\beta_1\beta_2) = \lambda^2$  because of  $\alpha_{12} = \alpha_{21}$  and thus Eq. 4.5 equals that in [56] after some appropriate linearizing.

In Fig. 4.4 the transition temperature  $T_I$  is presented as a function of the strontium fraction  $x = x_1 + x_2$ . For a fit of our data with equation 4.5 we took into account a constant contribution of Sr on tetragonal sites by setting  $x_1 = 0.29$ , which corresponds to about 72%, and  $x_3 = 1 - x$ . The fit yields  $\lambda = 0.51$ ,  $T_1^{tetr}(Sr) = T_2^{pent}(Sr) = 304K$  and  $T_3(Ba) = 668K$ , respectively. Allowing  $T_1^{tetr}(Sr) \neq T_2^{tetr}(Sr)$  simply results in an additional parameter without improving the quality of the fit. This means that constant polarization contributions like Sr on tetragonal sites or Niobium-Oxygen octahedra are implicitly included by an appropriate change of the temperature constants. Therefore the temperatures given should be regarded as fit parameters only. A  $\lambda$  less than 1 means that in this mixed system the coupling strength between the sub-lattices is weaker than the average value of the coupling strength within each sublattice. Such a reduction may be



due to random internal strain fields in the crystal lattice introduced by the different ionic sizes of Sr and Ba.

# Chapter 5

## Conclusions and Summary

The main contributions of this dissertation are summarized as follows:

- Often the determination of the band edge (energy or wavelength corresponding to a certain absorption coefficient) for polarized light absorption as a function of composition is useful for a nondestructive determination of the composition of a crystal. But in the case of SBN it is not a useful method because we found a non monotonic dependence of the band edge on the composition. This phenomenon is known as band gap bowing and the coefficient of the quadratic term ( $b$ ) is known as the bowing parameter.

To fit the temperature dependence of the band edge, a single oscillator has been used and we obtain the maximum slope for the congruent SBN crystal. Also the parameter  $E_g(0)$  reflects the band bowing.

- The infrared  $\text{OH}^-$  stretch mode absorption of various  $\text{Sr}_x\text{Ba}_{1-x}\text{Nb}_2\text{O}_6$  crystals with  $x$  ranging from 0.38 to 0.79 has been measured after increasing the proton concentration by a heat treatment in wet oxygen. A crystal with  $x = 0.79$  incorporates three times more hydrogen than one with  $x = 0.38$ . The shape of the spectra depends on the composition  $x$ . The spectra have been modelled using three components, two of them with fixed frequency while the third broad band decreases with increasing  $x$ . The three bands have been assigned to  $\text{OH}^-$  vibrations in the a,b plane of the crystal along the O-O bonds with different length and different cation environments.
- Raman spectra for all available compositions of SBN and all (non-equivalent) scattering configurations have been measured at room temperature. Composition-dependent

features are easiest to observe from A1 modes recorded in the X(ZZ)Y scattering geometry. A deconvolution of the band at about  $630\text{ cm}^{-1}$  results in two components, which are assigned to vibrations of different  $\text{NbO}_6$ -octahedra. Also the distortion of the  $\text{NbO}_6$  octahedra ( $\Delta[\text{Nb-O}]$ ) increases with the  $[\text{Sr}]/[\text{Ba}]$  concentration ratio in pentagonal channels.

- For a determination of the phase transition temperature we used pyroelectric measurements. The temperature of the relaxor phase-transition is determined from the inflexion point of the curve of the ferroelectric polarization versus temperature. The non linearity of the phase transition temperature dependence as a function of the  $[\text{Sr}]/[\text{Ba}]$  ratio can be explained by a system of three different sublattices at the crystallographic positions of Sr and Ba atoms.

# Appendix A

## Dielectric spectroscopy

Dielectric spectroscopy measures the dielectric permittivity as a function of frequency and temperature. It can be applied to all non-conducting materials. The frequency range extends over nearly 18 orders of magnitude: from the  $\mu\text{Hz}$  to the THz range close to the infrared region. Dielectric spectroscopy is sensitive to dipolar species as well as localized charges in a material, it determines their strength, their kinetics and their interactions. Thus, dielectric spectroscopy is a powerful tool for the electrical characterization of non-conducting or semiconducting materials in relation to their structure and also of electronic or sensor devices.

For dielectric measurements we build the setup that is presented in Fig. A.1. With a thermoelement, a sensor and a temperature controller (CAL3300 from CAL Controls), we can set the expected temperature of the sample with an accuracy of  $0.1\text{ }^{\circ}\text{C}$  in the range  $-10\text{ }^{\circ}\text{C}$  to  $280\text{ }^{\circ}\text{C}$ . For obtaining this temperature interval we used two kind of heaters: Peltier element and resistance.

Another component of the setup is a Lock-in amplifier. Lock-in amplifiers are used to measure the amplitude and phase of signals buried in noise. They achieve this by acting as a narrow bandpass filter which removes much of the unwanted noise while allowing to pass the signal which is to be measured.

The frequency of the signal to be measured and hence the passband region of the filter is set by a reference signal, which has to be supplied to the Lock-in amplifier along with the unknown signal. The reference signal must be at the same frequency as the modulation of the signal to be measured.

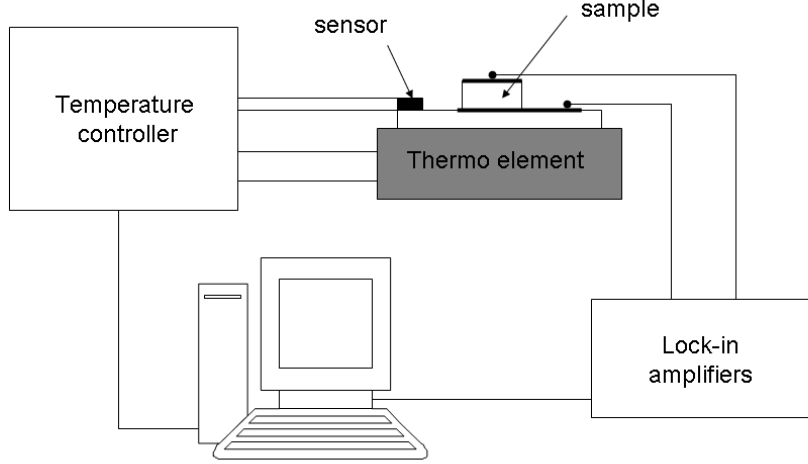


Figure A.1: Bloc diagram of the dielectric measurements setup

In our measurements we used a SR830 Digital Lock-in amplifier. The internal oscillator of the Lock-in amplifier generated the signal with a voltage  $U_0$  between 4 mV and 5 V and a frequency range from 1 mHz to 102 kHz.

For the capacity measurements the circuit presented in Fig. A.2 is used. At first a reference capacity is measured,  $C_r^*$  obtaining the values  $U_r^* = U_r' + iU_r''$ . After replacing this capacity with the sample  $C_s^*$  a second measurement will yield  $U_s^* = U_s' + iU_s''$ . The value of the sample capacity  $C_s^*$  is obtained using relation A.1

A.1.

$$C_s^* = C_r^* \frac{U_s^*(U_r^* - U_0)}{U_r^*(U_s^* - U_0)} \quad (\text{A.1})$$

where the  $U_0$  is the generated signal of the Look-in system.

In Fig. A.3 some results of capacity measurements of a SBN crystal are presented, which are in a good agreement with values reported in the literature.

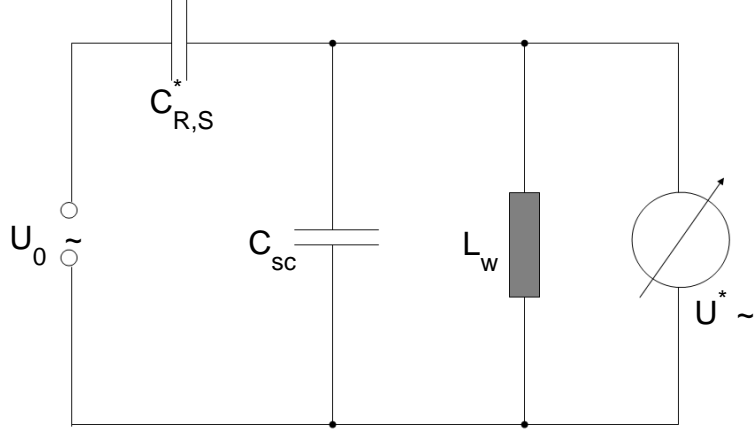


Figure A.2: Schematics of the dielectric measurements setup

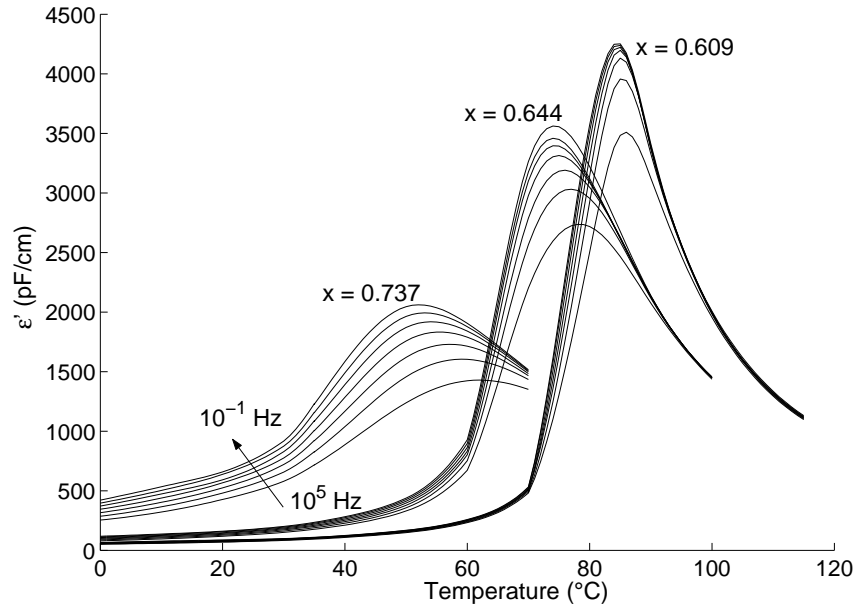


Figure A.3: Dependence of the dielectric constant (real part  $\epsilon'$ ) with temperature for different compositions in SBN.

# Bibliography

- [1] A. A. Ballman and H. Brown. The growth and properties of strontium barium metaniobate,  $\text{Sr}_{1-x}\text{Ba}_x\text{Nb}_2\text{O}_6$ , a tungsten bronze ferroelectric. *Journal of Crystal Growth*, 1:311, 1967.
- [2] M. R. Kruer, L. Esterowitz, F. J. Bartoli, and R. E. Allen. Optical radiation damage of sbn materials and pyroelectric detectors at  $10.6\ \mu\text{m}$ . *Journal of Applied Physics*, 46:1074, 1975.
- [3] A. M. Glass. Investigation of the electrical properties of  $\text{Sr}_{1-x}\text{Ba}_x\text{Nb}_2\text{O}_6$  with special reference to pyroelectric detection. *Journal of Applied Physics*, 40:4699, 1969.
- [4] J. B. Thaxter. Electric control of holographic storage in strontium-barium-niobate. *Applied Physics Letters*, 15:210, 1969.
- [5] J. B. Thaxter and M. Kestigian. Unique properties of SBN and their use in a layered optical memory. *Applied Optics*, 13:913, 1974.
- [6] F. Micheron, C. Mayeux, and J. C. Trotier. Electrical control in photoferroelectric materials for optical storage. *Applied Optics*, 13:784, 1974.
- [7] S. Redfield and L. Hesselink. Enhanced nondestructive holographic readout in strontium barium niobate. *Optical Letter*, 13:880, 1988.
- [8] H. Y. Zhang, X. H. He, Y. H. Shih, and L. Yan. Picosecond phase conjugation and two-wave coupling in strontium barium niobate. *Journal of Modern Optics*, 41:669, 1994.
- [9] M. Wesner, C. Herden, R. Pankrath, D. Kip, and P. Moretti. Temporal development of photorefractive solitons up to telecommunication wavelengths in SBN. *Physical Review E*, 64:36613, 2001.

- [10] A. S. Kewitsch<sup>1</sup>, M. Segev, A. Yariv, G. J. Salam, T. W. Towe, E. J. Sharp, and R. R. Neurgaonkar. Tunable quasi-phase matching using dynamic ferroelectric domain gratings induced by photorefractive space-charge fields. *Applied Physics Letters*, 64:3068, 1994.
- [11] J. M. Marx, Z. Tang, O. Eknayan, H. F. Taylor, and R. R. Neurgaonkar. Low-loss strain induced optical waveguides in strontium barium niobate  $\text{Sr}_{0.6}\text{Ba}_{0.4}\text{Nb}_2\text{O}_6$  at 1.3  $\mu\text{m}$  wavelength. *Applied Physics Letters*, 66:274, 1995.
- [12] M. Ulex, R. Pankrath, and K. Betzler. Growth of strontium barium niobate: the liquidus solidus phase diagram. *Journal of Crystal Growth*, 2004.
- [13] Johan Bergquist. *Two-Photon Absorption and Photorefraction in Semiconductors and Ferroelectrics*. Göteborg, 1994.
- [14] P. B. Jamieson, S. C. Abrahams, and J. L. Bernstein. Ferroelectric tungsten bronze-type crystal structures: I. barium strontium niobate  $\text{Ba}_{0.27}\text{Sr}_{0.75}\text{Nb}_2\text{O}_{5.78}$ . *Journal of Chemical Physics*, 48:5048, 1968.
- [15] A. E. Andreichuk, L. M. Dorozhkin, Yu. S. Kuzminov, I. A. Maslyanitsun, V. N. Molchanov, A. A. Rusakov, V. I. Simonov, V. D. Shigorin, and G. P. Shipulo. Quadratic optical susceptibility and structure of  $\text{Ba}_x\text{Sr}_{1-x}\text{Nb}_2\text{O}_6$  crystals. *Soviet Physics-Crystallography*, 29:641–645, 1984.
- [16] T. S. Chernaya, B. A. Maksimov, I. V. Verin, L. I. Ivleva, and V. I. Simonov. Crystal structure of  $\text{Ba}_{0.39}\text{Sr}_{0.61}\text{Nb}_2\text{O}_6$  single crystals. *Crystallography Reports*, 42:375–380, 1997.
- [17] M. P. Trubelja, E. Ryba, and D. K. Smith. A study of positional disorder in strontium barium niobate. *Journal of Materials Science*, 31:1435–1443, 1996.
- [18] T. S. Chernaya, B. A. Maksimov, T. R. Volk, L. I. Ivleva, and V. I. Simonov. Atomic structure of  $\text{Sr}_{0.75}\text{Ba}_{0.25}\text{Nb}_2\text{O}_6$  single crystal and composition-structure-property relation in  $(\text{Sr},\text{Ba})\text{Nb}_2\text{O}_6$  solid solutions. *Physics of the Solid State*, 42:1716–1721, 2000.
- [19] M. Ulex. *Züchtung und Charakterisierung von  $\text{Sr}_{1-x}\text{Ba}_x\text{Nb}_2\text{O}_6$ -Kristallen im Bereich von  $0,32 < x < 0,82$* . Universität Osnabrück, Dissertation, 2004.



- [20] C. David, T. Granzow, A. Tunyagi, M. Wöhlecke, Th. Woike, K. Betzler, M. Ulex, M. Imlau, and R. Pankrath. Composition dependence of the phase transition temperature in  $\text{Sr}_{1-x}\text{Ba}_x\text{Nb}_2\text{O}_6$ . *Solid State Physics (a)*, 291:R49–R52, 2004.
- [21] L. Kovács, G. Ruschhaupt, K. Polgár, G. Corradi, and M. Wöhlecke. Composition dependence of the ultraviolet absorption edge in lithium niobate. *Applied Physics Letters*, 70:2801, 1997.
- [22] Ch. Bäumer, C. David, A. Tunyagi, K. Betzler, H. Hesse, E. Krätzig, and M. Wöhlecke. Composition dependence of the ultraviolet absorption edge in lithium tantalate. *Journal of Applied Physics*, 93:3102, 2003.
- [23] J. A. Van Vechten and T. K. Bergstresser. Electronic structures of semiconductor alloys. *Physical Review B*, 1:3351, 1970.
- [24] Alex Zunger and J. E. Jaffe. Structural origin of optical bowing in semiconductor alloys. *Physical Review Letters*, 51:662, 1983.
- [25] James E. Bernard and Alex Zunger. Electronic structure of ZnS, ZnSe, ZnTe, and their pseudobinary alloys. *Physical Review B*, 36:3199, 1987.
- [26] J. Seglins and S. Kapphan. Huge shift of fundamental electronic absorption edge in  $\text{Sr}_{1-x}\text{Ba}_x\text{Nb}_2\text{O}_6$  crystals at elevated temperatures. *Physica Status Solidi (b)*, 188:43, 1995.
- [27] V. S. Vikhnin, S. Kapphan, and J. Seglins. Temperature induced red shift of the UV fundamental absorption edge in ferroelectric oxide crystals: Effect of charge transfer vibronic excitations. *Journal of the Korean Physical Society*, 32:621, 1998.
- [28] M. Meyer, M. Wöhlecke, and O. F. Schirmer. On the temperature dependence of the band edge of  $\text{Sr}_{0.61}\text{Ba}_{0.39}\text{Nb}_2\text{O}_6$ . *Physica Status Solidi (b)*, 221:1, 2000.
- [29] D. Redfield and W. J. Burke. Optical absorption edge of  $\text{LiNbO}_3$ . *Journal of Applied Physics*, 45:4566, 1974.
- [30] S. R. Johnson and T. Tiedje. Temperature dependence of the Urbach edge in GaAs. *Journal of Applied Physics*, 78:5609, 1995.
- [31] M. Wöhlecke and L. Kovács.  $\text{OH}^-$  ions in oxide crystals [review]. *Critical Reviews in Solid State & Materials Sciences*, 26:1–86, 2001.

- [32] S. Hunsche, A. Gröne, G. Greten, S. Kapphan, R. Pankrath, and J. Seglins. OH/OD-IR absorption bands in  $\text{Sr}_x\text{Ba}_{1-x}\text{Nb}_2\text{O}_6$ . *Physica Status Solidi A-Applied Research*, 148:629–634, 1995.
- [33] M. Lee, H. S. Lee, and R. S. Feigelson. Infrared OH-absorptions in  $\text{Sr}_{0.61}\text{Ba}_{0.39}\text{Nb}_2\text{O}_6$  crystals. *Journal of Applied Physics*, 84:1558–1560, 1998.
- [34] M. Gao. *Optical Investigation of Light-induced Charge Transport in SBN Crystals*. Universität Osnabrück, Dissertation, 1998.
- [35] M. K. Lee, H. Lee, R. K. Route, and R. S. Feigelson. Optical properties of lead barium niobate  $\text{Pb}_{1-x}\text{Ba}_x\text{Nb}_2\text{O}_6$  crystals. *Journal of Applied Physics*, 81:917–923, 1997.
- [36] M. Lee, R. S. Feigelson, A. Liu, L. Hesselink, and R. K. Route. Measurements of  $\text{OH}^-$  absorption and proton activation in  $\text{Pb}_{1-x}\text{Ba}_x\text{Nb}_2\text{O}_6$  crystals with applications to holographic storage. *Physical Review B*, 56:7898–7904, 1997.
- [37] Y. B. Kim, T. A. Kim, C. S. Kim, J. N. Kim, and J. H. Ro.  $\text{OH}^-/\text{OD}^-$  stretching vibration mode of ferroelectric  $\text{Li}_{1-x}\text{K}_x\text{NbO}_3$  ( $x = 0.05 - 0.6$ ). *Journal of the Korean Physical Society*.
- [38] T. H. Kim, Y. M. Yu, K. Lee, and J. H. Ro. Infrared  $\text{OH}^-$  absorption bands in potassium lithium niobate single crystals. *Physica Status Solidi (b)*, 227:485–490, 2001.
- [39] E. Libowitzky. Correlation of  $\text{O} - \text{H}$  stretching frequencies and  $\text{O} - \text{H} \cdots \text{O}$  hydrogen bond lengths in minerals. *Monatshefte für Chemie*, 130:1047–1059, 1999.
- [40] T. Hahn. *International Tables for Crystallography, Vol. A: Space-Group Symmetry*. 1983.
- [41] H. R. Xia, L. X. Li, H. Yu, X. L. Meng, L. Zhu, and L. J. Hu. Raman and infrared spectra of Nd-doped barium sodium niobate crystals. *Crystal Research and Technology*, 34:901, 1999.
- [42] H. R. Xia, H. Yu, H. Yang, K. X. Wang, B. Y. Zhao, J. Q. Wei, J. Y. Wang, and Y. G. Liu. Raman and infrared reflectivity spectra of potassium lithium niobate single crystals. *Physical Review B*, 55:14892, 1997.
- [43] R. Loudon. The Raman effect in crystals. *Advances in Physics*, 13:423, 1964.

- [44] E. Amzallag, T. S. Chang, R. H. Pantell, and R. S. Feigelson. Raman scattering by  $\text{Sr}_x\text{Ba}_{1-x}\text{Nb}_2\text{O}_6$ . *Journal of Applied Physics*, 42:3254, 1971.
- [45] R. E. Wilde. Raman spectrum of  $\text{Sr}_x\text{Ba}_{1-x}\text{Nb}_2\text{O}_6$ . *Journal of Raman Spectroscopy*, 22:321, 1991.
- [46] G. Burns, J. D. Axe, and D. F. O’Kane. Raman measurements of  $\text{NaBa}_2\text{Nb}_5\text{O}_{15}$  and related ferroelectrics. *Solid State Communications*, 7:933, 1969.
- [47] R. F. Schaufele and M. J. Weber. Raman scattering by lithium niobate. *Physical Review*, 152:705, 1966.
- [48] H. E. Puthoff, R. H. Pantell, B. G. Huth, and M. A. Chacon. Near-forward Raman scattering in  $\text{LiNbO}_3$ . *Journal of Applied Physics*, 39:2144, 1968.
- [49] M. E. Lines and A. M. Glass. *Principles and Applications of Ferroelectrics and Related Materials*. Clarendon Press Oxford, Oxford, 1977.
- [50] W. H. Huang, D. Viehland, and R. R. Neurgaonkar. Anisotropic glasslike characteristics of strontium barium niobate relaxors. *Journal of Applied Physics*, 76:490–496, 1994.
- [51] H. Arndt, T. V. Dung, and G. Schmidt. Domain-like structures in strontium barium niobate. *Ferroelectrics*, 97:247–254, 1989.
- [52] G. A. Smolenskij, V. A. Isupov, A. I. Agranovskaya, and S. N. Popov. *Soviet Physics Solid State*, 2:2584, 1961.
- [53] J. Dec, W. Kleemann, T. Woike, and R. Pankrath. Phase transitions in  $\text{Sr}_{0.61}\text{Ba}_{0.39}\text{Nb}_2\text{O}_6\text{:Ce}^{3+}$ : I. susceptibility of clusters and domains. *European Physical Journal B*, 14:627–632, 2000.
- [54] T. S. Chernaya, B. A. Maksimov, I. A. Verin, L. I. Ivleva, and V. I. Simonov. *Crystallography Reports*, 43:986–990, 1998.
- [55] J. A. Gonzalo. *Effective Field Approach to Phase Transitions and Some Applications to Ferroelectrics*. World Scientific Press, Singapore, 1991.
- [56] R. A. Ali, C. L. Wang, M. Yuan, Y. X. Wang, and W. L. Zhong. Compositional dependence of the Curie temperature in mixed ferroelectrics: effective field approach. *Solid State Communications*, 129:365–367, 2004.

## Acknowledgements

I owe my deepest gratitude to my supervisor apl. Prof. Dr. Manfred Wöhlecke, for guiding me in the world of science. His enthusiasm and optimistic attitude towards research and life in general have inspired me during these years. I learned a lot from numerous stimulating discussions with him in the the past three years. He has given me an exceptional opportunity to carry out the present work. The support and help of Prof. Wöhlecke were not limited to the scientific supervision, but have extended to many problems of a daily life.

I wish to express my sincere gratitude to apl. Prof. Klaus Betzler for his guidance and support. From Prof. Betzler I obtained a lot of skills and helps in experiments. I also should thank for his help in many problems related to electronics and programming language (Visual C++ and MATLAB).

I thank Dr. Rainer Pankrath and Dr. Michael Ulex for a large amount of SBN crystals.

I thank my colleagues Dr. Arthur Tunyagi and Dipl.-Phys. Isabella-Ioana Oprea for useful collaboration and friendly encouragements.

I would like to thank Junior-Prof. Mirco Imlau for useful advice connected with my work.

I would like to thank Mrs. Gerda Cornelsen, Mr. Gregor Steinhoff and Dr. Wolfgang Mikosch who helped me in various ways.

I would like to acknowledge the financial support from the Graduate College *Nonlinearities of Optical Materials*, financed by the Deutsche Forschungsgemeinschaft and the Federal State of Niedersachsen.